Received: 14 December 2018 | Revised: 18 October 2019 | Accepted: 30 December 2019

DOI: 10.1002/navi.353

ORIGINAL ARTICLE

WILEY ION

A new array concept using spatially distributed subarrays for unambiguous GNSS interference mitigation in automotive applications

Marius Brachvogel[1] | **Michael Niestroj**[1] | **Soeren Zorn**[1] | **Michael Meurer**[1,2] | **Syed N. Hasnain**[3] | **Ralf Stephan**[3] | **Matthias A. Hein**[3]

[1]Chair of Navigation, RWTH Aachen University, Aachen, Germany

[2]Institute of Communications and Navigation, German Aerospace Center (DLR), Weßling, Germany

[3]RF & Microwave Research Group, Technische Universitaet Ilmenau, Ilmenau, Germany

Correspondence
Marius Brachvogel, Chair of Navigation, RWTH Aachen, Mies-van-der-Rohe-Str. 15, Aachen 52074, Germany.
Email: marius.brachvogel@nav.rwth-aachen.de

Funding information
Bundesministerium für Wirtschaft und Energie, Grant/Award Number: 50 NA 1717, 50 NA 1718, 50 NA 1901 and 50 NA 1902

Abstract

Radio frequency interference (RFI) poses a severe problem for conventional GNSS receivers. Even low powered RFI can block the reception of satellite signals and prevent a position determination. Antenna array systems have been proven suitable to counteract RFI by incorporating spatial processing techniques. The large size of uniform rectangular arrays (URA) with half-wave antenna spacing impedes an installation in cars intended for the consumer mass market, where a hidden installation is a strict requirement by industry and customers.

This paper introduces a new approach, where a conventional URA is split into distributed linear subarrays with the aim to reduce their footprint but to maintain the possibility of spatial processing. The achievable gain in robustness against RFI is evaluated. Drawbacks in terms of manifold ambiguities and their consequences for spatial processing techniques are also discussed. Furthermore, the accuracy of positioning results derived from a field test is put into context with a single antenna receiver.

1 | INTRODUCTION

Global navigation satellite systems (GNSS) play a crucial role in our daily routine, as they provide access to the only globally available system to determine an absolute position. This paper puts the focus on the automotive area with the scope on highly automated driving, where a reliable and robust positioning service is indispensable. According to recent research in this field of application, the position solution is likely to be delivered by a multisensor approach in the near future, thereby fusing GNSS observables with the data from highly accurate sensors, such as RADAR, LiDAR, and camera-based solutions, which are available in many cars even today. GNSS thereby provides the absolute but coarse position estimation that can be refined through the relative but highly accurate sensor data. For that purpose, this paper emphasizes a code-based position solution with the focus on robustness against RF interference (RFI) sources. Due to the low power of the received satellite signals, conventional GNSS receivers are prone to RFI degrading the accuracy of the receiver or even impeding signal reception. With the increasing number of GNSS applications, the deliberate transmission of RFI, also known as jamming, has attracted attention in past years.[1] Therefore, antenna arrays have proven as an effective countermeasure.[2] They extend the degrees of freedom of RFI mitigation to the spatial domain using techniques such as beam steering or null steering, thereby facilitating

the possibility to attenuate the direction of arrival (DOA) of an impinging RFI. Additionally, the signal to noise ratio (SNR) of the satellite signals can be increased with the same approach.[3] Those techniques rely on the relative phase delays that an impinging signal experiences following from the different positions of the radiating elements. In order to avoid unwanted attenuation of desired signals or amplification of interfering signals, respectively, care must be taken in the array design to avoid ambiguities in the array manifold. Therefore, the structure of conventional arrays is typically chosen as a grid, where the element spacing in each direction does not exceed half of a carrier wavelength. A common example is the uniform rectangular array (URA). Hence, the optimum size of a square 2×2 URA is to a certain degree linked to the physical properties of the incident wave. This leads to typical sizes of such URA of 25 cm × 25 cm for the GNSS frequency ranges of interest. The size of a URA therefore impedes its application in the consumer automotive sector, where aesthetic design is of paramount importance and a hidden installation is required by the automotive OEMs. This paper therefore investigates the novel idea of breaking up such a large antenna array into several subarrays and of distributing those among the car at suitable positions in order to cope with the limited mounting space. Doing so, compared to classical single antenna receivers even in the case of strong interference, a reliable position estimation should be provided. At the aforementioned positions, the car body must be transparent to GNSS signals. The resulting spacing among the subarrays is typically much larger than half of the wavelength and, therefore, may cause ambiguities in the array manifold. We describe a technique to avoid the detrimental consequences of such ambiguities and to exploit distributed arrays for robust satellite navigation.

The paper is structured as follows. Following Section 2, which describes the system model and the beamforming algorithms employed, Section 3 focuses on the uniqueness of the overall array manifold based on position and orientation of the subarrays: It emphasizes a design rule to avoid ambiguities in the DOA estimation for one dominant incident signal[4] on a steering vector-based manifold model. Their impact is demonstrated for the example of interference mitigation of the receiver, and the consequences for the satellite signal processing are discussed. Furthermore, a comparison with the steering vector-based manifold of a typical half-wave URA is illustrated.

The metallic car body in the near field of the antenna system raises further challenges, as especially the power levels of the incident signal can no longer be assumed equal in all antenna channels. Therefore, Section 4 shows measurements of the gain and phase of the proposed array pattern evaluated in the measurement chamber *Virtual Road - Simulation and Test Area* (VISTA)[5] at the TU Ilmenau. Consequences of the increased dimensions of the resulting array on its beamforming capability due to signal decorrelation at the distributed antennas resulting from the car body, signal delay, and platform rotations are discussed in Section 5. To proof the possibility of an incorporation of beamforming algorithms using the proposed array and furthermore to evaluate their performance in a realistic scenario, satellite signals are captured with two subarrays mounted to the front bumper of a car. The accuracy of the position results derived from the combination of antenna signals displaced by several wavelengths are assessed in Section 6 and put into context with the results of a single antenna receiver on top of the car. Finally, the benefit of the proposed solution to deliver a global position even in heavily interfered environments is demonstrated.

2 | SIGNAL MODEL

In the following, we assume a planar array of N antenna elements at fixed positions as shown in Figure 1. The analytical signal of the ith source impinging at a virtual ideal isotropic antenna element at the origin is denoted as

$$c^i(t) = c^i_{\mathrm{b}}(t) \cdot \mathrm{e}^{\mathrm{j}2\pi f^i_{\mathrm{r}} t}, \tag{1}$$

which is composed of an arbitrary baseband signal $c^i_{\mathrm{b}}(t)$ modulated onto a carrier signal defined through the received carrier frequency

$$f^i_{\mathrm{r}} \approx f_{\mathrm{t}} + f^i_{\mathrm{d}} = f_{\mathrm{t}} \cdot \left(1 + \frac{v^i}{c_0}\right), \tag{2}$$

which consists of the transmit frequency f_{t} and the additive received Doppler f^i_{d} depending on the relative velocity

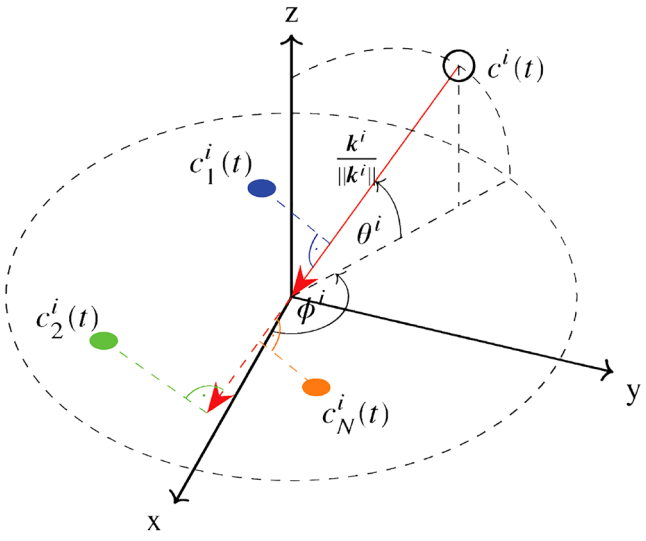

FIGURE 1 Coordinate system, normalized wave vector, and relative delays to the origin for a narrowband source signal incident from $\phi^i = 150°$ and $\theta^i = 40°$ [Color figure can be viewed at wileyonlinelibrary.com and www.ion.org]

v^i of the source and speed of light c_0. It is assumed that the array is located in the far field of the transmitting antenna, such that the incident wave is approximately planar. The position of an arbitrary antenna element n in the xy-plane can be described as

$$\boldsymbol{r}_n(t) = r_n(t) \cdot \begin{pmatrix} \cos\phi_n(t) \\ \sin\phi_n(t) \\ 0 \end{pmatrix}, \tag{3}$$

where $\phi_n(t)$ is the angle to the nth antenna at time t in the xy-plane as shown in Figure 1. The signal received from this antenna element can be described using Equation (1) as

$$\begin{aligned} c_n^i(t) &= \gamma_n(t) \cdot c^i\left(t - \tau_n^i(t)\right) \\ &= \gamma_n(t) \cdot c_{\mathrm{b}}^i\left(t - \tau_n^i(t)\right) \cdot \mathrm{e}^{\mathrm{j}2\pi f_{\mathrm{r},n}^i(t)\cdot\left(t-\tau_n^i(t)\right)} \end{aligned} \tag{4}$$

which differs compared to the signal in the origin by a position dependent delay $\tau_n^i(t)$, a velocity dependent additive Doppler $f_{\mathrm{r},n}^i(t)$, and $\gamma_n(t)$ describing the component influence on amplitude and phase. Using the wave vector

$$\boldsymbol{k}\left(\phi^i, \theta^i\right) = -\frac{2\pi f_{\mathrm{r}}^i}{c_0}\begin{pmatrix} \cos\phi^i\cos\theta^i \\ \sin\phi^i\cos\theta^i \\ \sin\theta^i \end{pmatrix} = \frac{2\pi f_{\mathrm{r}}^i}{c_0} \cdot \boldsymbol{e}_{\boldsymbol{k}}^i, \tag{5}$$

which describes the wave propagation in Cartesian coordinates, the temporal offset of the signal of the nth antenna element depending on the direction of arrival of the signal relative to the orientation of the receiver is calculated by

$$\tau_n^i(t) = \frac{1}{c_0}\boldsymbol{r}_n^{\mathrm{T}}(t) \cdot \boldsymbol{e}_{\boldsymbol{k}}^i. \tag{6}$$

The additional Doppler depending on the antenna array movement can be calculated using its instantaneous orientation and the constant direction of the carrier signal as

$$f_{\mathrm{r},n}^i(t) \approx f_{\mathrm{r}}^i + f_{\mathrm{d},n}^i(t) = f_{\mathrm{t}} + f_{\mathrm{d}}^i - f_{\mathrm{t}} \cdot \frac{\dot{\boldsymbol{r}}_n^{\mathrm{T}}(t) \cdot \boldsymbol{e}_{\boldsymbol{k}}^i}{c_0}, \tag{7}$$

where $\dot{\boldsymbol{r}}_n(t) = \boldsymbol{v}_n(t)$ denotes the velocity of the antenna element relative to the direction of the incident signal. Please note that the received Doppler shift is composed of a common Doppler shift for all antenna elements f_{d}^i associated with the Doppler frequency for the virtual reference antenna at the origin as denoted in Equation (1) and a differential Doppler shift due to the relative movement of the individual antenna elements $f_{\mathrm{d},n}^i(t)$ with respect to the origin. The vector containing the signals of all antenna elements as defined in Equation (4) can be described as

$$\begin{aligned} \boldsymbol{c}^i(t) = \underbrace{\boldsymbol{\gamma}\left(\phi_{\mathrm{r}}^i(t), \theta_{\mathrm{r}}^i(t)\right) \odot \begin{pmatrix} \mathrm{e}^{-\mathrm{j}2\pi f_{\mathrm{r},1}^i(t)\tau_1^i(t)} \\ \mathrm{e}^{-\mathrm{j}2\pi f_{\mathrm{r},2}^i(t)\tau_2^i(t)} \\ \vdots \\ \mathrm{e}^{-\mathrm{j}2\pi f_{\mathrm{r},N}^i(t)\tau_N^i(t)} \end{pmatrix}}_{\boldsymbol{a}^i(t)} \\ \odot \begin{pmatrix} c_{\mathrm{b}}^i\left(t-\tau_1^i(t)\right) \\ c_{\mathrm{b}}^i\left(t-\tau_2^i(t)\right) \\ \vdots \\ c_{\mathrm{b}}^i\left(t-\tau_N^i(t)\right) \end{pmatrix} \odot \begin{pmatrix} \mathrm{e}^{\mathrm{j}2\pi f_{\mathrm{d},1}^i(t)\cdot t} \\ \mathrm{e}^{\mathrm{j}2\pi f_{\mathrm{d},2}^i(t)\cdot t} \\ \vdots \\ \mathrm{e}^{\mathrm{j}2\pi f_{\mathrm{d},N}^i(t)\cdot t} \end{pmatrix} \cdot \mathrm{e}^{\mathrm{j}2\pi f_{\mathrm{r}}^i t}, \end{aligned} \tag{8}$$

where $\odot$ denotes the Hadamard product and $\boldsymbol{\gamma}\left(\phi_{\mathrm{r}}^i(t), \theta_{\mathrm{r}}^i(t)\right)$ collecting the hardware-dependent influence on the overall received amplitude and phase through antennas and analog front-end, which are dependent on the time-varying direction of arrival of signal i. The signals differ between the antenna elements by a time-varying phase offset defined through the product of instantaneous delay and received frequency, a delay between the baseband signals, and different Doppler frequencies concerning the carrier.

Considering a stationary example with $\boldsymbol{r}_n(t) = \boldsymbol{r}_n$, it follows that $\tau_n^i(t) = \tau_n^i$ and $f_{\mathrm{d},n}^i(t) = 0$. Thus, Equation (8) becomes

$$\boldsymbol{c}^i(t) = \boldsymbol{a}(\phi_{\mathrm{r}}^i, \theta_{\mathrm{r}}^i) \odot \begin{pmatrix} c_{\mathrm{b}}^i\left(t-\tau_1^i\right) \\ c_{\mathrm{b}}^i\left(t-\tau_2^i\right) \\ \vdots \\ c_{\mathrm{b}}^i\left(t-\tau_n^i\right) \end{pmatrix} \cdot \mathrm{e}^{\mathrm{j}2\pi f_{\mathrm{r}}^i \cdot t}, \tag{9}$$

which defines the array manifold vector[6] as

$$\boldsymbol{a}\left(\phi_{\mathrm{r}}^i, \theta_{\mathrm{r}}^i\right) = \boldsymbol{\gamma}\left(\phi_{\mathrm{r}}^i, \theta_{\mathrm{r}}^i\right) \odot \begin{pmatrix} \mathrm{e}^{-\mathrm{j}\boldsymbol{k}^{\mathrm{T}}\left(\phi^i,\theta^i\right)\boldsymbol{r}_1} \\ \mathrm{e}^{-\mathrm{j}\boldsymbol{k}^{\mathrm{T}}\left(\phi^i,\theta^i\right)\boldsymbol{r}_2} \\ \vdots \\ \mathrm{e}^{-\mathrm{j}\boldsymbol{k}^{\mathrm{T}}\left(\phi^i,\theta^i\right)\boldsymbol{r}_N} \end{pmatrix}, \quad \boldsymbol{a}\left(\phi, \theta\right) \in \mathbb{C}^{N\times 1}, \tag{10}$$

where the latter consists of the array steering vector describing the influence of the spatial separation of the radiating elements and ϕ_{r}^i and θ_{r}^i correspond to the direction of arrival relative to the receiver orientation. Using Equation (9), it is apparent, that assuming a quasi-stationary example, the difference between the received signals of a pair of two antenna elements p and q can be expressed by a constant signal delay $\tau_p^i - \tau_q^i$, which converts to a phase offset in terms of the carrier signal. As only GNSS signals from the upper hemisphere are of interest, Equation (10) can be used to formulate the array manifold on the corresponding bounded domains of ϕ and θ as[7]

$$\mathcal{A} = \left\{\boldsymbol{a}\left(\phi, \theta\right) | 0° \le \phi < 360°, 0° \le \theta \le 90°\right\}, \tag{11}$$

which describes the overall impact on amplitude and phase depending on ϕ and θ through an N-dimensional complex plane.

2.1 | Spatial signal processing

Let's consider a GNSS receiver with n antenna elements. The vector describing the received signals is denoted by

$$\begin{aligned}\boldsymbol{x}(t) &= \begin{pmatrix} x_1(t) \\ x_2(t) \\ \vdots \\ x_N(t) \end{pmatrix} = \boldsymbol{s}(t) + \boldsymbol{z}(t) + \boldsymbol{n}(t) \\ &= \sum_L \boldsymbol{s}^l(t) + \sum_M \boldsymbol{z}^m(t) + \boldsymbol{n}(t), \qquad \boldsymbol{x}(t) \in \mathbb{C}^{N\times 1},\end{aligned} \tag{12}$$

which is a superposition of L useful satellite signals, M interference signals, and additive noise $\boldsymbol{n}(t)$. In the following, it is assumed that $\boldsymbol{n}(t)$ is spatially and temporally zero-mean white Gaussian noise. The contribution of the lth satellite to the received signal $\boldsymbol{x}(t)$ of Equation (12) is described with Equation (8) as

$$\boldsymbol{s}^l(t) = \boldsymbol{a}^l(t) \odot \begin{pmatrix} s_\mathrm{b}^l\left(t - \tau_1^l(t)\right) \\ s_\mathrm{b}^l\left(t - \tau_2^l(t)\right) \\ \vdots \\ s_\mathrm{b}^l\left(t - \tau_N^l(t)\right) \end{pmatrix} \odot \begin{pmatrix} \mathrm{e}^{\mathrm{j}2\pi f_{\mathrm{d},1}^l(t)\cdot t} \\ \mathrm{e}^{\mathrm{j}2\pi f_{\mathrm{d},2}^l(t)\cdot t} \\ \vdots \\ \mathrm{e}^{\mathrm{j}2\pi f_{\mathrm{d},N}^l(t)\cdot t} \end{pmatrix} \cdot \mathrm{e}^{\mathrm{j}2\pi f_\mathrm{r}^l t}, \tag{13}$$

where $\boldsymbol{a}^l(t)$ collects the hardware influences $\boldsymbol{\gamma}(t)$ and the time-dependent steering vector. The baseband signals $s_\mathrm{b}^l(t) = \sqrt{P^l} \cdot p^l(t) \cdot d^l(t)$, where P^l is the signal power, consist of the pseudo-random noise (PRN) sequence for code division multiple access (CDMA) and the data signal. Analogously, the mth undesired interference signal is given as

$$\boldsymbol{z}^m(t) = \boldsymbol{a}^m(t) \odot \begin{pmatrix} z_\mathrm{b}^m\left(t - \tau_1^m(t)\right) \\ z_\mathrm{b}^m\left(t - \tau_2^m(t)\right) \\ \vdots \\ z_\mathrm{b}^m\left(t - \tau_N^m(t)\right) \end{pmatrix} \odot \begin{pmatrix} \mathrm{e}^{\mathrm{j}2\pi f_{\mathrm{d},1}^m(t)\cdot t} \\ \mathrm{e}^{\mathrm{j}2\pi f_{\mathrm{d},2}^m(t)\cdot t} \\ \vdots \\ \mathrm{e}^{\mathrm{j}2\pi f_{\mathrm{d},N}^m(t)\cdot t} \end{pmatrix} \cdot \mathrm{e}^{\mathrm{j}2\pi f_\mathrm{r}^m t} \tag{14}$$

where $z_\mathrm{b}^m(t)$ denotes an arbitrary baseband signal inside the receiver bandwidth. In the following, the signals $\boldsymbol{x}[k] = \boldsymbol{x}(k/f_\mathrm{s})$, $\boldsymbol{s}[k] = \boldsymbol{s}(k/f_\mathrm{s})$, and $\boldsymbol{z}[k] = \boldsymbol{z}(k/f_\mathrm{s})$ with $k \in \mathbb{Z}$ denote the demodulated and digitized signals using the center frequency f_t and the sampling rate f_s, respectively.

2.1.1 | Pre-correlation beamforming

As a countermeasure against interference signals and to amplify the weak received GNSS signals, a blind two-stage beamforming technique[3] as depicted in Figure 2 is proposed and analyzed in this paper. This technique detects and estimates incident signals without further information using only their correlation before and after PRN despreading. The interference mitigation stage works on blocks of K samples of the digitized antenna signals defined as

$$\begin{aligned}\boldsymbol{X}[\kappa] &= \left(\boldsymbol{x}[\kappa], \boldsymbol{x}[\kappa+1], \ldots, \boldsymbol{x}[\kappa+K-1]\right), \\ \boldsymbol{X}[\kappa] &\in \mathbb{C}^{N\times K}, \quad \kappa \in \mathbb{Z}, \quad K \in \mathbb{N},\end{aligned} \tag{15}$$

where the window index κ points to an arbitrary sample in the digitized antenna signal $\boldsymbol{x}[k]$.

The interference mitigation block in Figure 2 calculates the spatial covariance among the raw antenna signals using one block of data of Equation (15). The covariance matrix of an arbitrary block yields

$$\begin{aligned}\boldsymbol{R}_{\mathrm{xx}}[\kappa] &= \boldsymbol{X}[\kappa] \cdot \boldsymbol{X}^\mathrm{H}[\kappa] \\ &\approx \boldsymbol{R}_{\mathrm{ss}}[\kappa] + \boldsymbol{R}_{\mathrm{zz}}[\kappa] + \boldsymbol{R}_{\mathrm{nn}}[\kappa], \qquad \boldsymbol{R}_{\mathrm{xx}}[\kappa] \in \mathbb{C}^{N\times N}\end{aligned} \tag{16}$$

where $\boldsymbol{R}_{\mathrm{ss}}[\kappa]$, $\boldsymbol{R}_{\mathrm{zz}}[\kappa]$, and $\boldsymbol{R}_{\mathrm{nn}}[\kappa]$ denote the spatial covariance matrices of the discrete satellite, interference, and

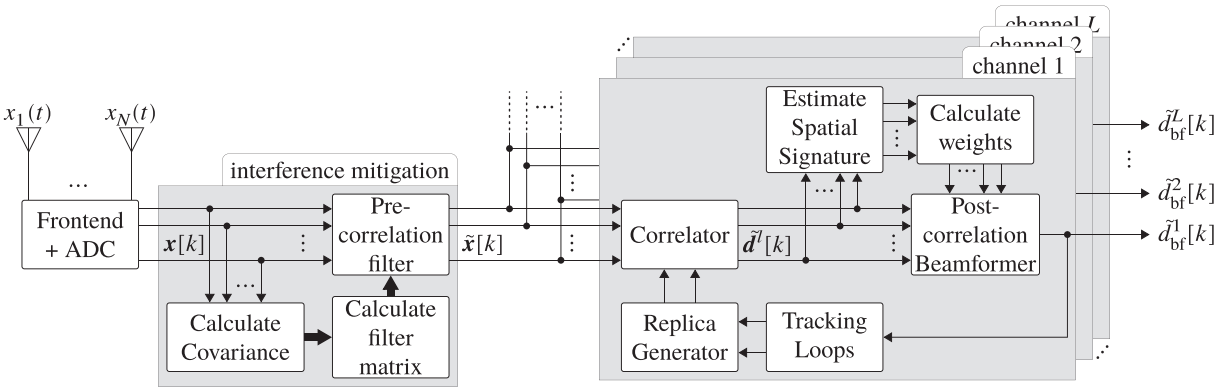

FIGURE 2 Block diagram of the considered beamforming algorithms: Potential interferences are mitigated by decorrelating the raw antenna signals. The satellite signals are independently amplified after demodulation and despreading using the correlator outputs of the tracking channels

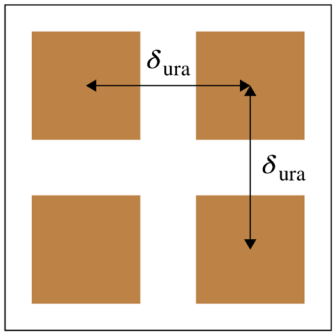

(A) Conventional uniform rectangular array

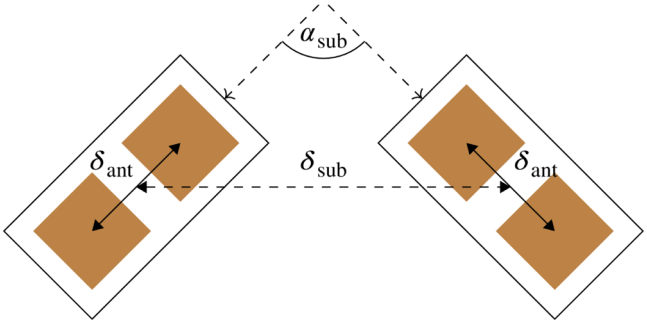

(B) Combination of two linear sub-arrays

FIGURE 3 Illustration of the array topologies under comparison [Color figure can be viewed at wileyonlinelibrary.com and www.ion.org]

noise blocks, which are defined according to Equation (15) for the signal components $\boldsymbol{s}[k]$, $\boldsymbol{z}[k]$, and $\boldsymbol{n}[k]$, respectively. $\boldsymbol{R}_{\text{ss}}[\kappa]$ and $\boldsymbol{R}_{\text{zz}}[\kappa]$ can further be expressed as

$$\boldsymbol{R}_{\text{ss}}[\kappa] = \boldsymbol{A}_{\text{s}}[\kappa]\boldsymbol{R}_{\text{s's'}}[\kappa]\boldsymbol{A}_{\text{s}}^{\text{H}}[\kappa], \tag{17}$$

$$\boldsymbol{R}_{\text{zz}}[\kappa] = \boldsymbol{A}_{\text{z}}[\kappa]\boldsymbol{R}_{\text{z'z'}}[\kappa]\boldsymbol{A}_{\text{z}}^{\text{H}}[\kappa]. \tag{18}$$

where

$$\boldsymbol{A}_{\text{s}}[\kappa] = \left[\boldsymbol{a}\left(\phi_{\text{r}}^{1}[\kappa], \theta_{\text{r}}^{1}[\kappa]\right), \ldots, \boldsymbol{a}\left(\phi_{\text{r}}^{L}[\kappa], \theta_{\text{r}}^{L}[\kappa]\right)\right] \tag{19}$$

$$\boldsymbol{A}_{\text{z}}[\kappa] = \left[\boldsymbol{a}\left(\phi_{\text{r}}^{1}[\kappa], \theta_{\text{r}}^{1}[\kappa]\right), \ldots, \boldsymbol{a}\left(\phi_{\text{r}}^{M}[\kappa], \theta_{\text{r}}^{M}[\kappa]\right)\right] \tag{20}$$

denote the steering matrices and $\boldsymbol{R}_{\text{s's'}}[\kappa]$ and $\boldsymbol{R}_{\text{z'z'}}[\kappa]$ are $N \times N$ matrices of satellite and interference signal powers, respectively. It is assumed that the cross-correlation terms among the different signal components $\boldsymbol{s}[k]$, $\boldsymbol{z}[k]$, and $\boldsymbol{n}[k]$ are negligible. Since the power of GNSS signals is well below the thermal noise floor of the receiver, Equation (16) can be approximated to

$$\boldsymbol{R}_{\text{xx}}[\kappa] \approx \boldsymbol{R}_{\text{zz}}[\kappa] + \boldsymbol{R}_{\text{nn}}[\kappa] = \boldsymbol{R}_{\text{nn}}[\kappa] + \sigma_n^2\boldsymbol{I}, \tag{21}$$

where σ_n^2 denotes the variance of the signals in the spatially white thermal noise vector $\boldsymbol{n}[k]$ and $\boldsymbol{I}$ is the identity matrix. Thereby it is assumed that the block length K is chosen large enough such that $\boldsymbol{n}[k]$ can be modeled as wide-sense stationary over the interval defined in Equation (15). Furthermore it is assumed that in case of strong crosstalk in the front-end, such that the assumption of spatial white noise in the digitized signals is no longer justified, a suitable calibration method is incorporated.[8] A common approach to mitigate interference signals is to use a scaled inverse of the interference covariance matrix to derive the spatial precorrelation filter $\boldsymbol{P}$,[3] eg,

$$\tilde{\boldsymbol{x}}[k] = \boldsymbol{P}[\kappa] \cdot \boldsymbol{x}[k] = \frac{\sqrt{N}}{\|\boldsymbol{R}_{\text{xx}}^{-\alpha}[\kappa]\|_{\text{F}}} \cdot \boldsymbol{R}_{\text{xx}}^{-\alpha}[\kappa] \cdot \boldsymbol{x}[k], \tag{22}$$

where $\|\cdot\|_{\text{F}}$ denotes the Frobenius norm and $0 < \alpha \leq 1$ in order to attenuate the spatially correlated interference. In this paper, the so-called *prewhitening filter* with $\alpha = \frac{1}{2}$ is used to decorrelate the antenna signals.

2.1.2 | Post-correlation beamforming

Complementary to spatially mitigating the DOAs of interference signals, the post-correlation beamformer aims at amplifying signals from spatial directions of the satellite signals. The output of correlator l can be denoted as

$$\tilde{\boldsymbol{d}}^{l}[k] = p^{l}\left[k; \tau_{\text{c}}\right] \cdot \tilde{\boldsymbol{x}}[k], \tag{23}$$

where τ_{c} denotes the current delay for the correlator tap. A spatial filter optimizing the signal to interference and noise ratio (SINR) of satellite l is given by

$$\tilde{d}_{\text{bf}}^{l}[k] = \boldsymbol{w}^{\text{H}}\left[\kappa_{\text{c}}\right] \cdot \tilde{\boldsymbol{d}}^{l}[k] = \hat{\boldsymbol{u}}_{\tilde{\text{d}}}^{\text{H}}\left[\kappa_{\text{c}}\right] \cdot \tilde{\boldsymbol{d}}^{l}[k], \tag{24}$$

where the window index κ_{c} points to an arbitrary block of K_{c} samples in $\tilde{\boldsymbol{d}}^{l}[k]$. $\hat{\boldsymbol{u}}_{\tilde{\text{d}}}\left[\kappa_{\text{c}}\right]$ is the eigenvector corresponding to the largest eigenvalue of $\boldsymbol{R}_{\tilde{\text{d}},\tilde{\text{d}}}\left[\kappa_{\text{c}}\right]$ which is derived after Equation (16) from the data block

$$\tilde{\boldsymbol{D}}^{l}\left[\kappa_{\text{c}}\right] = \left[\tilde{\boldsymbol{d}}^{l}\left[\kappa_{\text{c}}\right], \tilde{\boldsymbol{d}}^{l}\left[\kappa_{\text{c}}+1\right], \ldots, \tilde{\boldsymbol{d}}^{l}\left[\kappa_{\text{c}}+K_{\text{c}}-1\right]\right]. \tag{25}$$

The quality of the post-correlation beamformer is highly dependent on the estimation of $\hat{\boldsymbol{u}}_{\tilde{\text{d}}}$. Therefore, multipath signals may seriously affect the quality of signal amplification and thus lead to an increased error in pseudorange. For a scenario in which NLOS signals are dominant, a multipath mitigation algorithm[9] must be incorporated to reduce this effect and ensure the quality of the beamformer formulated in Equation (24). As the interference mitigation stage as well as the post-correlation beamformer both

estimate the direction of an incident signal blindly using its phase differences in the antenna channels and attenuate or amplify the signal, respectively, each possible DOA must translate through Equation (10) to a unique vector in the array manifold of Equation (11). Therefore, care has to be taken by the choice of the antenna positions $\boldsymbol{r}_1$ to $\boldsymbol{r}_N$, as those are the only influenceable parameters during the array design.

3 | ARRAY DESIGN

To cope with the few and limited mounting spaces in a car that are transparent to GNSS signals, the size of a URA as illustrated in Figure 3A has to be reduced at least in one dimension. Since a further miniaturization is difficult to achieve and evokes other problems, such as mutual coupling of the antenna elements or increased beamwidth, a distribution of single elements or groups of subarrays is of interest in this section that maintains the performance of the URA as far as possible. This distribution poses a problem for the beamforming algorithms, as an adverse choice of the antenna positions can lead to ambiguities in the manifold $\mathcal{A}$. As the beamforming algorithms evaluate the phase difference between the antenna channels, the direction-dependent hardware influence $\boldsymbol{\gamma}(\phi, \theta)$ introduced by the antenna elements is assumed stationary and thus neglected in this section. The impact of ambiguities raised through an adverse choice of the antenna positions on the interference mitigation algorithm is therefore discussed on a steering vector based manifold for an array consisting of groups of linear subarrays.

3.1 | Rank-one ambiguities

Under the assumption $\boldsymbol{\gamma}(\phi, \theta) = 1$, Equation (11) states that the manifold is an N-dimensional complex function depending on the antenna positions, the carrier frequency, and the angular domains of ϕ and θ. Since the latter two are in general non-variable parameters, the only degree of freedom on $\mathcal{A}$ is given by the antenna positions. The design of a URA is generally bound to the constraint that the edge length, ie, the distance between two antenna elements on the array edge δ_{ura}, does not exceed half of a carrier wavelength, ie,

$$0 < \delta_{\text{ura}} \leq \frac{\lambda}{2}, \tag{26}$$

where λ is the wavelength of the incident signal. This constraint ensures that $\mathcal{A}_{\text{ura}}$ is free of so-called ambiguities for the domains of ϕ and θ as defined in Equation (11). A rank-one ambiguity is defined as a manifold vector $\boldsymbol{a}(\phi, \theta)$,

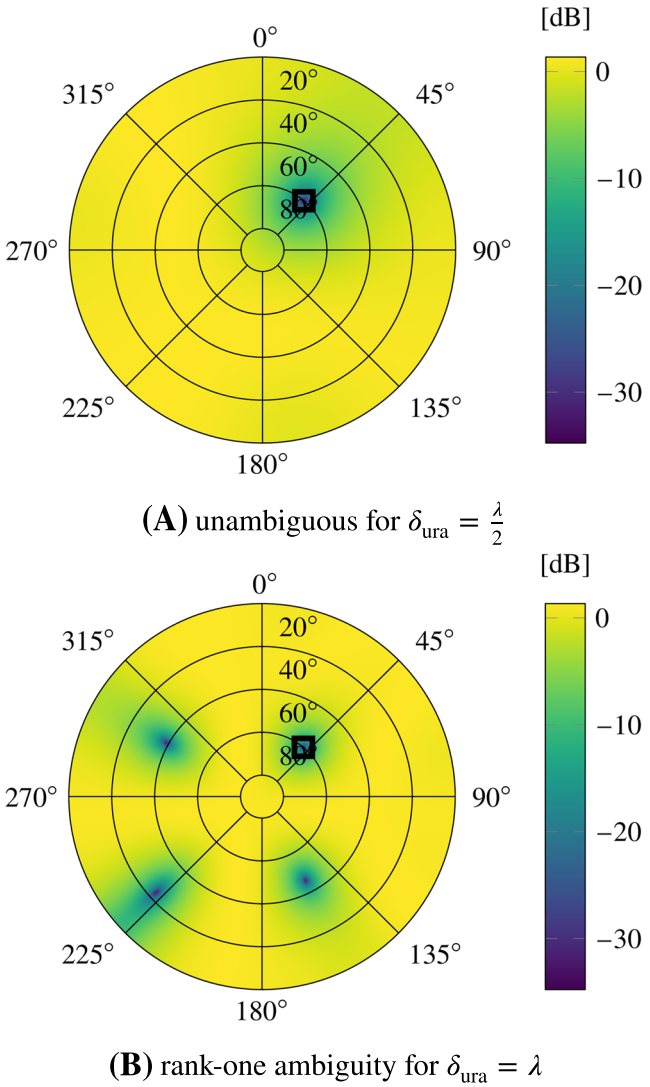

FIGURE 4 Comparison of the interference mitigation capability between two 2×2 URAs as illustrated in Figure 3A with different edge lengths δ_{ura} for a single stationary interference signal $z(t)$ (■) with a power of 30 dB above the thermal noise floor of the antennas and incident from $\phi^z = 40°$ and $\theta^z = 60°$ [Color figure can be viewed at wileyonlinelibrary.com and www.ion.org]

which appears repeatedly in $\mathcal{A}$ for at least two different directions of arrival as

$$\boldsymbol{a}\left(\phi^p, \theta^p\right) = g \cdot \boldsymbol{a}\left(\phi^q, \theta^q\right), \qquad \text{with} \quad \left(\phi^p, \theta^p\right) \neq \left(\phi^q, \theta^q\right), \tag{27}$$

where $g \in \mathbb{C}\backslash\{0\}$ is an arbitrary scalar factor. This is illustrated in Figure 4, where the influence of the interference mitigation filter is shown for two different example URAs for a single active interference source $z(t)$. The power of the interference signal in this and the following evaluations is arbitrarily chosen to be 30 dB above the thermal noise floor of the antenna elements, whereas the interference

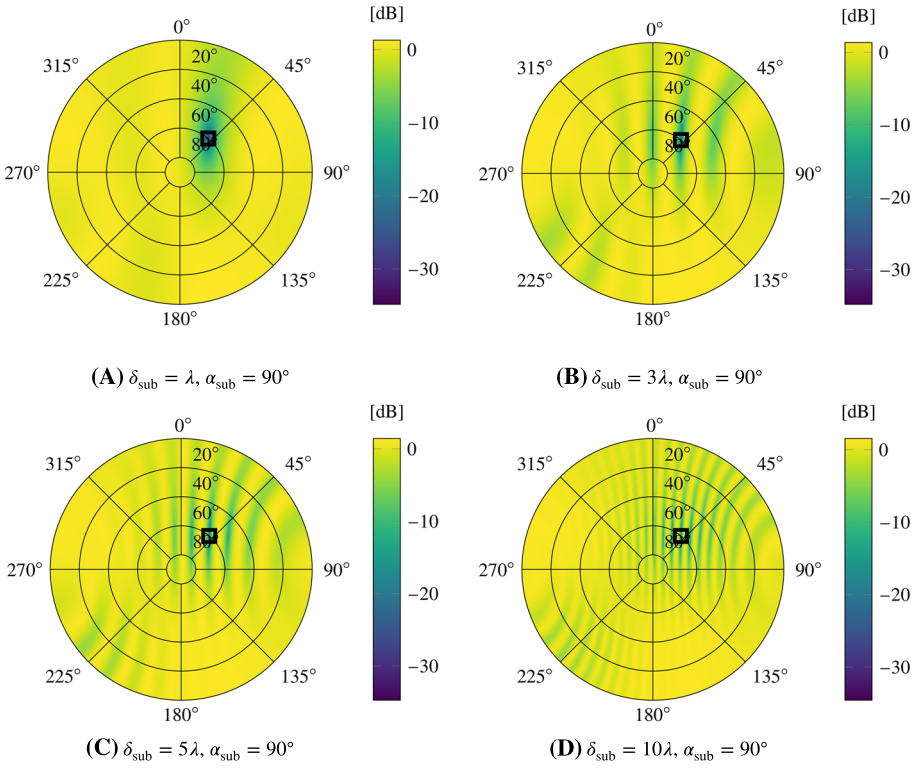

(A) $\delta_{\text{sub}} = \lambda$, $\alpha_{\text{sub}} = 90°$ **(B)** $\delta_{\text{sub}} = 3\lambda$, $\alpha_{\text{sub}} = 90°$

(C) $\delta_{\text{sub}} = 5\lambda$, $\alpha_{\text{sub}} = 90°$ **(D)** $\delta_{\text{sub}} = 10\lambda$, $\alpha_{\text{sub}} = 90°$

FIGURE 5 Influence of δ_{sub} for a fixed $\alpha_{\text{sub}} = 90°$ on the interference mitigation capability for a single interference source (■) [Color figure can be viewed at wileyonlinelibrary.com and www.ion.org]

DOA is selected to be constant at $\phi^z = 40°$ and $\theta^z = 60°$. In order to assess the impact of the precorrelation filter of Equation (22) on a received signal, an arbitrary impinging unit power signal with direction of arrival ϕ^i and θ^i is considered. The power of that signal at the output of the precorrelation filter can be written as

$$L\left(\phi^i, \theta^i\right) = \frac{1}{N^2} \cdot \boldsymbol{a}^{\mathrm{H}}\left(\phi^i, \theta^i\right) \cdot \boldsymbol{P}^{\mathrm{H}} \cdot \boldsymbol{P} \cdot \boldsymbol{a}\left(\phi^i, \theta^i\right). \quad (28)$$

Figure 4A shows the spatial attenuation for the case where the edge distance of the URA is chosen according to Equation (26) as $\delta_{\text{ura}} = \frac{\lambda}{2}$. The interference is perfectly mitigated, whereas other directions are scarcely influenced. In contrast, the impact of an URA with antenna positions violating the constraint from Equation (26) and thus leading to three rank-one ambiguities are presented in Figure 4B for $\delta_{\text{ura}} = \lambda$. The array cannot differentiate between the true interference DOA and three ambiguous directions. By mitigating the interference signal, those three other spatial directions are simultaneously suppressed.

A constraint to prevent rank-one ambiguities was defined in prior efforts[4,10,11]: Since the parameter space of $\mathcal{A}$ is defined by the two orthogonal parameters ϕ and θ in Equation (11), each has to be sampled through a combination of two antennas as a uniform linear array (ULA) as shown in Figure 3B. This is called a subarray in the following. Similar to the sampling rate f_{s} in the time domain, which must fulfill the Nyquist criterion $\lambda_{\text{s}} \leq \frac{\lambda_{\max}}{2}$, the distance between the antenna elements in a subarray must satisfy $\delta_{\text{ant}} \leq \frac{\lambda_{\max}}{2}$ in order to sample the phase difference of an incident wave unambiguously, where $\lambda_{\max}$ is determined through f_{r}. As the array resolution, ie, the width of the beam, is improved with an increased aperture, δ_{ant} is chosen to be $\frac{\lambda_{\max}}{2}$ in the following. The remaining parameters defining the combination of the two subarrays are the distance between the subarray center points δ_{sub} and the angle α_{sub} between the vectors parallel to each subarray as indicated in Figure 3B.

The influence of increasing values of δ_{sub} is visualized in Figure 5 for a fixed $\alpha_{\text{sub}} = 90°$: As the spatial separation between the subarrays increases, an increasing number of other spatial directions, which are located on arcs, are simultaneously attenuated. Possibly incident signals from those directions encounter less attenuation compared to the mitigated interference signal, but the reception of weak GNSS signals might be especially impaired. Since the beamwidth decreases for increasing δ_{sub} as demonstrated in Figure 5B-D, the spatial separation should be minimized to avoid signal decorrelation between the subarrays despite the improved spatial resolution. As the delays between the antenna elements as stated in Equation (8) increase, the correlation between the temporally shifted baseband signals in the antenna channels decreases depending on the autocorrelation function of $c_{\text{b}}(t)$ as stated in Equation (1).

This effect is dependent on the signal bandwidth f_b and affects the capability of the beamforming techniques to mitigate or amplify the signals, which could be compensated through the use of multiple correlators in the case of the satellite signals. However, for the precorrelation beamformer, this effect must be considered. A discussion including correlation losses through platform rotations follows in Section 5.

The influence of α_{sub} on the ambiguity of $\mathcal{A}_{sub}$ is shown in Figure 6 for a fixed $\delta_{sub} = \lambda$. As α_{sub} deviates from 90° to 0° so that the angle becomes more obtuse as shown for $\alpha_{sub} = 45°$ in Figure 6B, a second DOA is simultaneously attenuated, where the attenuation increases continuously for increasing deviation from $\alpha_{sub} = 90°$ until a true ambiguity is formed for $\alpha_{sub} = 0°$ as shown in Figure 6A. If α_{sub} varies in the other direction, ie, from $\alpha_{sub} = 90°$ to $\alpha_{sub} = 180°$, so that it becomes more acute, the attenuation is incrementally distributed over an arc, until the array becomes a ULA for $\alpha_{sub} = 180°$, which is ambiguous for the chosen parameter space by design.

3.2 | Higher-rank ambiguities

A rank-one ambiguity in $\mathcal{A}$ as defined in Equation (27) states that the array cannot differentiate between the direction of a single incident signal and another DOA. A rank-Q ambiguity is defined as

$$\boldsymbol{a}\left(\phi^p, \theta^p\right) = \sum_Q g^q \cdot \boldsymbol{a}\left(\phi^q, \theta^q\right) \quad \text{with } \left(\phi^p, \theta^p\right) \neq \left(\phi^q, \theta^q\right) \text{ and } q = 1, 2 \ldots, Q, \tag{29}$$

which means that there exist $Q + 1$ linearly dependent manifold vectors in $\mathcal{A}$. In that case, the superposition of Q signals, incident from distinct directions, leads to the erroneous mitigation of at least one additional DOA. There exist further design rules for different array topologies,[12,13] to avoid ambiguities up to a particular rank. Unfortunately, these rely on specific arrangements of the antenna elements, as, for example, a grid or cross structure, and are therefore not applicable in the case at hand, where size and

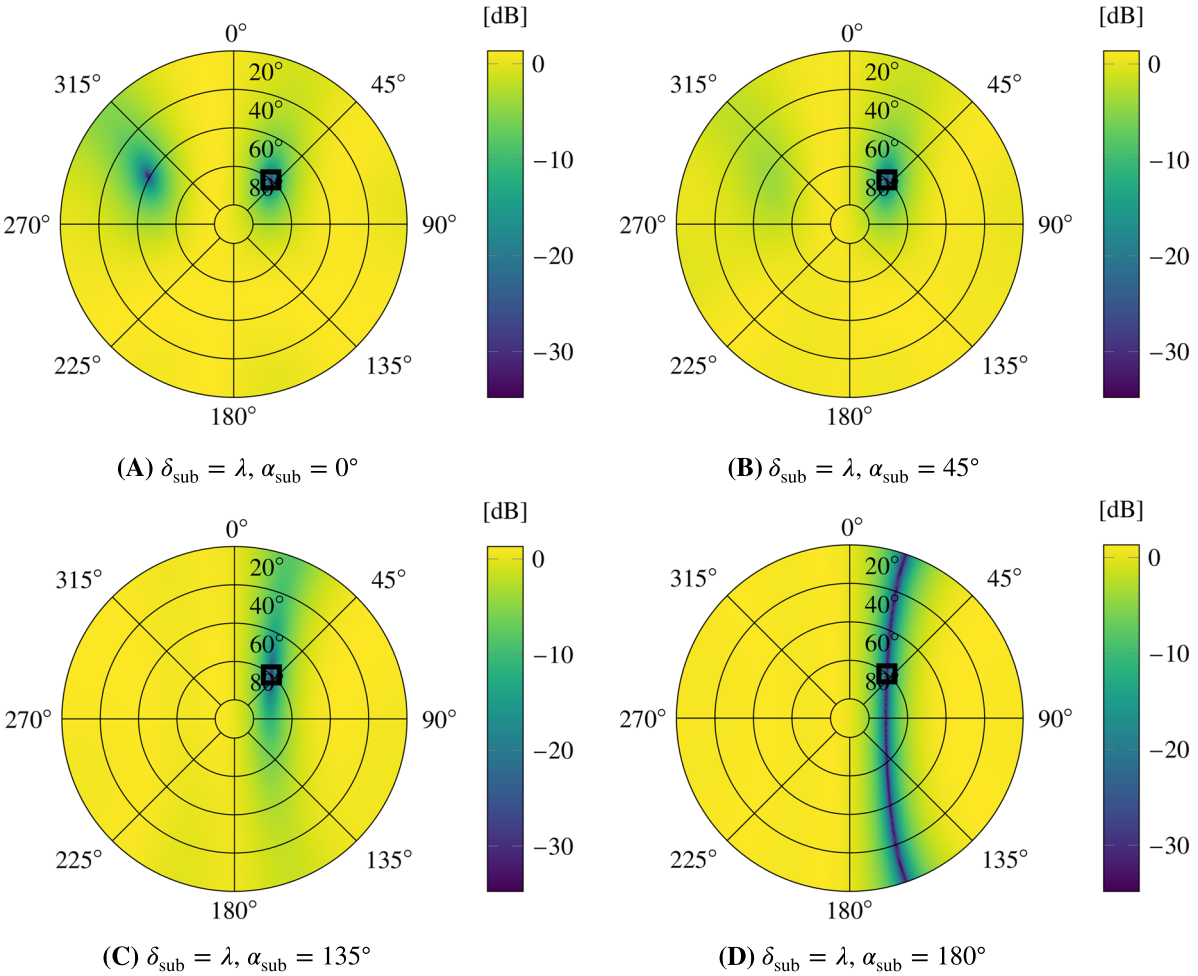

(A) $\delta_{sub} = \lambda$, $\alpha_{sub} = 0°$ **(B)** $\delta_{sub} = \lambda$, $\alpha_{sub} = 45°$

(C) $\delta_{sub} = \lambda$, $\alpha_{sub} = 135°$ **(D)** $\delta_{sub} = \lambda$, $\alpha_{sub} = 180°$

FIGURE 6 Influence of α_{sub} for $\delta_{sub} = \lambda$ on the interference mitigation capability for a single interference source (■) [Color figure can be viewed at wileyonlinelibrary.com and www.ion.org]

shape, and thereby the mounting places of the different subarrays, differ from car to car. Depending on the number of incident signals, there may occur ambiguities up to rank $(N-1)$.

4 | PROPOSED CONFIGURATION OF ANTENNA ARRAYS

The previous section analyzed the uniqueness of the spatial processing techniques on a steering vector based manifold model, ie, only depending on the choice of antenna positions and neglecting imperfections of analog components as well as the non-negligible influence of the metallic car body on the overall array manifold, which is included in $\boldsymbol{\gamma}(\phi, \theta)$ in Equation (10). This section presents measurements of gain and phase of an exemplary array configuration, thus providing an evaluation of the direction dependent signal quality at the distributed antenna elements. This is especially important, as the comparably low installation height, eg, in the bumpers, leads to attenuation or complete loss of signals incident from directions where the signal path is obstructed by the car body. As Equations (22) and (24) estimate the manifold vector through correlation between the antenna signals, they require the respective signal available in each antenna channel of the proposed array configuration in Figure 3B.

Therefore, the installation of two subarray combinations as illustrated in Figure 7A in the front and rear bumper, leading to a total number of eight antennas, is proposed as one potential configuration to achieve a full coverage of the upper hemisphere. To evaluate the influence of the car body on the received signal power, commercial patch antennas are mounted onto the car bumpers as shown in

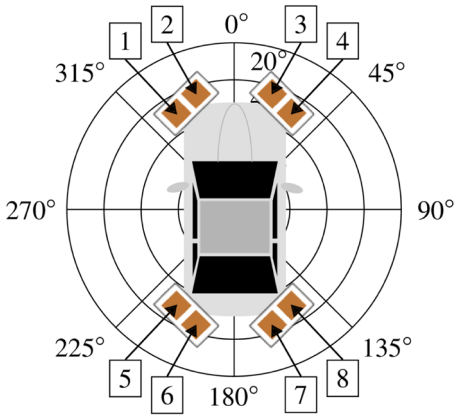

(A) Car installation and antenna identifier

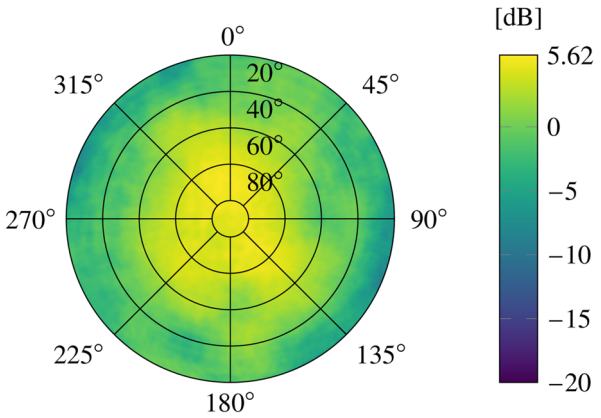

(B) Logarithmic realizable array gain $G(\phi, \theta)$ through optimal weighting as expressed in Equation (34)

FIGURE 7 Proposed subarray distribution over the car and achievable signal power [Color figure can be viewed at wileyonlinelibrary.com and www.ion.org]

(A) View on the front bumper installation (from left to right: antennas 4,3,2,1)

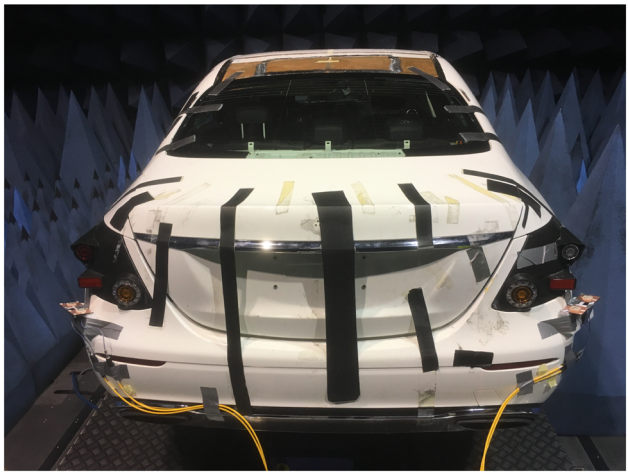

(B) View on the rear bumper installation (from left to right: antennas 5,6,7,8)

FIGURE 8 Subarray installation on front and rear bumper in the measurement chamber VISTA [Color figure can be viewed at wileyonlinelibrary.com and www.ion.org]

Figure 8, and the array manifold after Equation (11) is measured with a spatial resolution of 1° for ϕ and θ, ie,

$$\phi_{\mathrm{m}} = \left[0°, 1°, \ldots, 359°\right] \in \mathbb{N}^{1\times 360}, \tag{30}$$

$$\theta_{\mathrm{m}} = \left[0°, 1°, \ldots, 90°\right] \in \mathbb{N}^{1\times 91} \tag{31}$$

at the L1 center frequency of 1575.42 MHz in the measurement chamber VISTA[5] at the TU Ilmenau. The obtained manifold after Equation (11)

$$\mathcal{A}_{\mathrm{m}} = \{\boldsymbol{a}_{\mathrm{m}}(\phi_{\mathrm{m}}, \theta_{\mathrm{m}})\} \tag{32}$$

is normalized to the maximum amplitude measured at a single antenna, ie,

$$\max_{\forall \phi_{\mathrm{m}}, \theta_{\mathrm{m}}, n} \left| a_{\mathrm{m},n}(\phi_{\mathrm{m}}, \theta_{\mathrm{m}}) \right| = 1. \tag{33}$$

Therefore, the realizable gain through array processing compared to a single antenna receiver for a specific DOA, which can be achieved by applying the optimum weights after Equation (24) to the antenna channels, can be expressed by

$$G(\phi, \theta) = \boldsymbol{a}_{\mathrm{m}}^{\mathrm{H}}(\phi, \theta) \cdot \boldsymbol{a}_{\mathrm{m}}(\phi, \theta) = ||\boldsymbol{\gamma}(\phi, \theta)||_2^2, \tag{34}$$

where $\boldsymbol{a}_{\mathrm{m}}(\phi, \theta)$ represents the normalized measured manifold vector for an arbitrary DOA. This is expressed on a logarithmic scale in Figure 7B. However, this averages over the direction-dependent reception quality of all subarrays, which is expected to show significant differences at each subarray position.

To assess those, the realizable subarray gains, which can be used to evaluate the signal reception at each corner of the car, can be expressed by reformulating Equation (34) with the pth and qth entry of $\boldsymbol{a}_{\mathrm{m}}(\phi, \theta)$ for two arbitrary antennas as

$$G_{p,q}(\phi, \theta) = \left[a_{\mathrm{m},p}^{*}(\phi, \theta), \quad a_{\mathrm{m},q}^{*}(\phi, \theta) \right] \cdot \begin{bmatrix} a_{\mathrm{m},p}(\phi, \theta) \\ a_{\mathrm{m},q}(\phi, \theta) \end{bmatrix}, \tag{35}$$

where $(\cdot)^*$ denotes the complex conjugate. The results obtained by evaluating Equation (35) for the antenna pairs of each subarray are presented in Figure 9A-D. Each subarray receives about three-fourths of the upper hemisphere, whereas the signal paths, which are obstructed by the car, are strongly attenuated. Thereby it is ensured that each quarter of the hemisphere is redundantly covered by two subarray combinations from Figure 3B as proposed in Section 3. For example, the quadrant for $0° < \phi < 90°$ is covered by the combinations of the front left and front right subarray and the front right and rear right subarray. Note, that the lower bound of the gain information in Figures 7 and 9 is restricted to −20 dB for better visibility. The attenuation in the direction of the car body ranges between 30 and 40 dB and thus improves the robustness against interference sources further, as there is always one subarray, which receives the interference strongly attenuated. To present the influence of the analog components and the metallic car body on the received signal phase $\angle\gamma_n(\phi, \theta)$ for the nth antenna channel, it is necessary to remove the influence of the antenna positions from the measurement. In other words, to show $\angle\gamma_n(\phi, \theta)$ one has to remove the steering vector included in the measurement

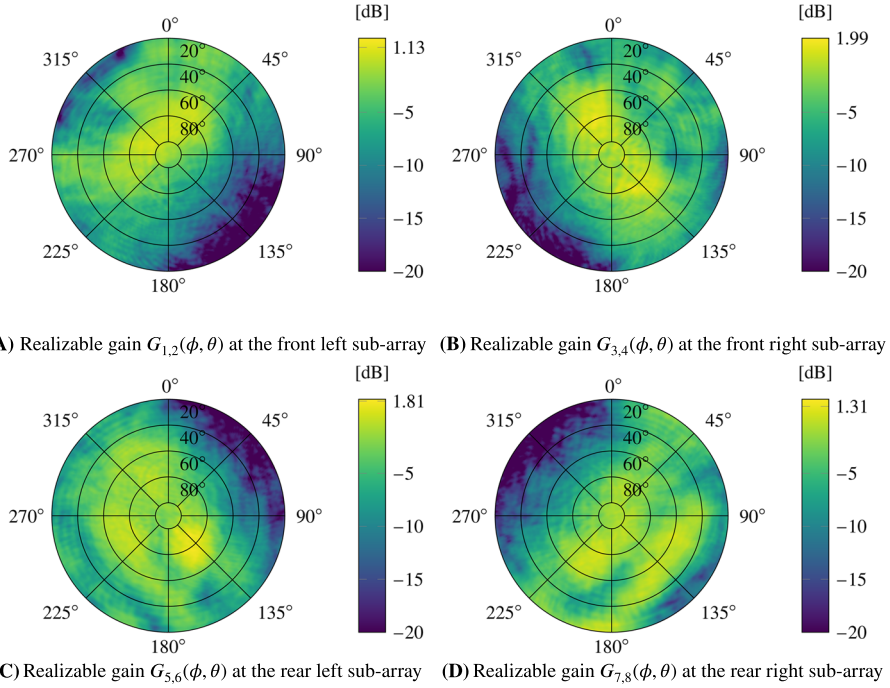

(A) Realizable gain $G_{1,2}(\phi, \theta)$ at the front left sub-array **(B)** Realizable gain $G_{3,4}(\phi, \theta)$ at the front right sub-array

(C) Realizable gain $G_{5,6}(\phi, \theta)$ at the rear left sub-array **(D)** Realizable gain $G_{7,8}(\phi, \theta)$ at the rear right sub-array

FIGURE 9 Influence of the car body on the received signal power at the individual subarrays on a logarithmic scale. The fractional values at the color bars denote the maximum value of the combined gain in the respective subfigure [Color figure can be viewed at wileyonlinelibrary.com and www.ion.org]

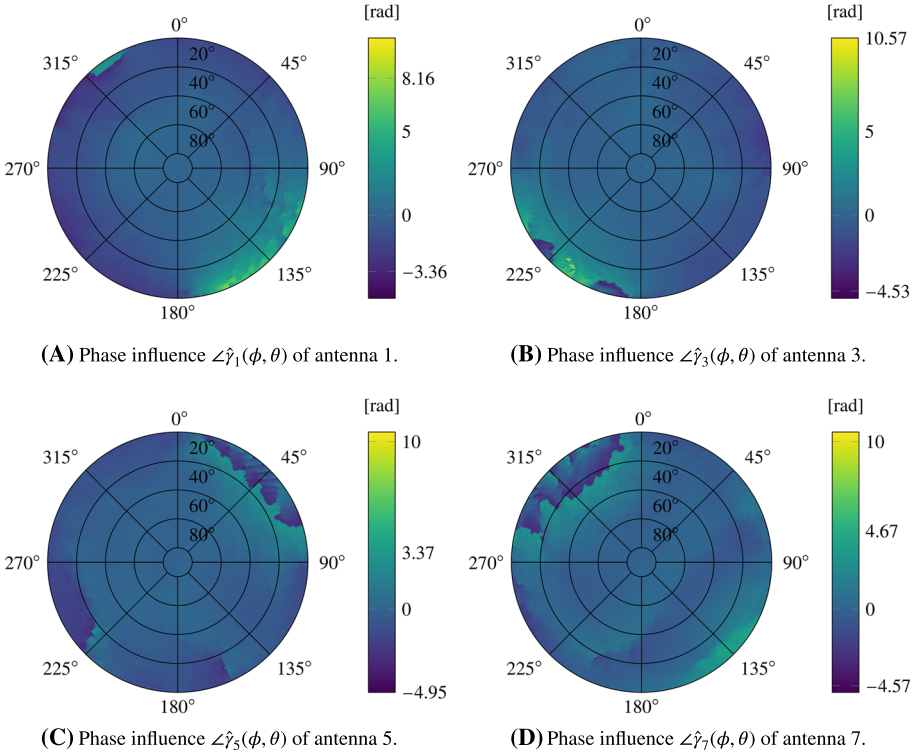

(A) Phase influence $\angle\hat{\gamma}_1(\phi,\theta)$ of antenna 1.

(B) Phase influence $\angle\hat{\gamma}_3(\phi,\theta)$ of antenna 3.

(C) Phase influence $\angle\hat{\gamma}_5(\phi,\theta)$ of antenna 5.

(D) Phase influence $\angle\hat{\gamma}_7(\phi,\theta)$ of antenna 7.

FIGURE 10 Phase influence $\angle\hat{\gamma}_n(\phi,\theta)$ at antennas 1, 3, 5, and 7. The fractional values at the color bars denote the minimum and maximum value of the phase measurement in the respective subfigure [Color figure can be viewed at wileyonlinelibrary.com and www.ion.org]

$\boldsymbol{a}_{\mathrm{m}}(\phi,\theta)$. As the antenna positions could not be accurately determined during the experiment, they must be estimated from the obtained manifold by solving the overdetermined set of linear equations for the measured phase defined after Equation (10)

$$\boldsymbol{K}^{\mathrm{T}} \cdot \begin{bmatrix} \hat{\boldsymbol{r}}_n \\ \hat{\varphi}_n \end{bmatrix} = \boldsymbol{\Phi}_{\mathrm{m},n} \tag{36}$$

through a least squares fit, where $\hat{\varphi}_n$ denotes an arbitrary phase offset and $\hat{\boldsymbol{r}}_n$ the aspired antenna positions. The vector

$$\begin{aligned} \boldsymbol{\Phi}_{\mathrm{m},n} = \big[&\angle a_{\mathrm{m},n}(\phi_{\mathrm{m}}[1],\theta_{\mathrm{m}}[46]),\ \ldots,\angle a_{\mathrm{m},n}(\phi_{\mathrm{m}}[360],\theta_{\mathrm{m}}[46]),\\ &\angle a_{\mathrm{m},n}(\phi_{\mathrm{m}}[1],\theta_{\mathrm{m}}[47]),\ \ldots,\angle a_{\mathrm{m},n}(\phi_{\mathrm{m}}[360],\theta_{\mathrm{m}}[91])\big]\\ &\text{with}\ \ \boldsymbol{\Phi}_{\mathrm{m},n} \in \mathbb{R}^{1\times 16560} \end{aligned} \tag{37}$$

contains the unwrapped measured phase information for antenna n with an elevation mask of 45°, which was found to minimize the residual from Equation (36). The matrix

$$\begin{aligned} \boldsymbol{K} = &\begin{bmatrix} \boldsymbol{k}\left(\phi_{\mathrm{m},n}[1],\theta_{\mathrm{m},n}[46]\right),\ \ldots,\boldsymbol{k}\left(\phi_{\mathrm{m},n}[360],\theta_{\mathrm{m},n}[91]\right) \\ 1,\ \ldots,1 \end{bmatrix}\\ &\text{with}\ \ \boldsymbol{K} \in \mathbb{R}^{4\times 16560} \end{aligned} \tag{38}$$

collects the wave vectors after Equation (5) corresponding to the angles in $\boldsymbol{\Phi}_{\mathrm{m},n}$. The resulting estimated antenna positions were found to be

$$\begin{aligned} \hat{\boldsymbol{r}}_1 &= \begin{bmatrix} -0.80 \\ 2.56 \\ 0.02 \end{bmatrix}, & \hat{\boldsymbol{r}}_2 &= \begin{bmatrix} -0.73 \\ 2.62 \\ 0.03 \end{bmatrix}, & \hat{\boldsymbol{r}}_3 &= \begin{bmatrix} 0.82 \\ 2.61 \\ -0.04 \end{bmatrix}, & \hat{\boldsymbol{r}}_4 &= \begin{bmatrix} 0.90 \\ 2.53 \\ -0.05 \end{bmatrix}\\ \hat{\boldsymbol{r}}_5 &= \begin{bmatrix} -0.78 \\ -1.93 \\ 0.02 \end{bmatrix}, & \hat{\boldsymbol{r}}_6 &= \begin{bmatrix} -0.71 \\ -2.01 \\ 0.04 \end{bmatrix}, & \hat{\boldsymbol{r}}_7 &= \begin{bmatrix} 0.86 \\ -1.96 \\ -0.01 \end{bmatrix}, & \hat{\boldsymbol{r}}_8 &= \begin{bmatrix} 0.93 \\ -1.91 \\ 0.03 \end{bmatrix}, \end{aligned} \tag{39}$$

which have been rounded to centimeters. The obtained positions fit well to the dimensions of the utilized car. The estimated phase influence $\angle\hat{\gamma}_n(\phi,\theta)$ at antenna n after removing the position-dependent phase as expressed through the steering vector from Equation (10) is plotted as an example for one antenna of each subarray in Figure 10. Similar to the received power shown in Figure 9, the phase information of signals incident from directions where the signal path is obstructed by the car body is distorted.

5 | CONSEQUENCES OF PLATFORM ROTATIONS ON BEAMFORMING CAPABILITIES

The beamformers as formulated in Equations (22) and (24) both assume a quasi-stationary context regarding an incident signal, where the fluctuations through Doppler and delay as described in Equation (8) can be neglected between the antenna channels during the observation

interval T_{obs}, such that the covariance matrices of incident signals can be modeled after Equation (17) and Equation (18), respectively.

Compared to compact arrays, this assumption raises demands on the utilized receiver bandwidth and the observation intervals K and K_{c} of Equations (22) and (24) as both, Doppler and delay lead to a loss of correlation between the antenna channels. The consequence is that a single strong incident signal evokes multiple additional non-zero eigenvalues instead of one in the estimation of the covariance matrix, which may be modeled as additional signal sources and affect the signal to noise and interference ratio. To analyze this effect, we assume a single incident interferer $z(t)$ in the following and express the signal to interference and noise ratio as[14]

$$\text{SINR}\left(\phi^i,\theta^i\right) = P\left(\phi^i,\theta^i\right)\cdot\sum_{q=0}^{N-1}\frac{\left|\boldsymbol{a}_{\text{m}}^{\text{H}}\left(\phi^i,\theta^i\right)\cdot A_{\text{x},q}\right|^2}{\lambda_q}, \quad (40)$$

where $A_{\text{x},q}$ is the eigenvector corresponding to the qth eigenvalue λ_q of the covariance matrix defined in Equation (21) and $P\left(\phi^i,\theta^i\right)$ is the transmission power of the signal of interest incident from that DOA. Note that the following analysis only evaluates the behavior of the eigenvalues depending on the signal bandwidth f_{b} and the differential receiver-motion dependent Doppler $f_{\text{d},n}$ and thus also holds in case of satellite signals. Equation (40) states that an increase of the ith eigenvalue further decreases the SINR and thus causes a loss in beamformer performance.

By formulating and rearranging the expected value between a pair of two arbitrary antenna elements p and q, eg, the entry at line p and column q of the covariance matrix defined after Equation (16), as

$$\begin{aligned}
&\text{E}\left[\left(c_p^i(t)\right)^*\cdot c_q(t)\right]\\
=\;&\text{E}\left[\gamma_p^*(t)\cdot\left(c_{\text{b}}^i\left(t-\tau_p^i(t)\right)\right)^*\cdot \text{e}^{-\text{j}2\pi f_{\text{r},p}^i(t)t}\cdot\text{e}^{\text{j}2\pi f_{\text{r},p}^i(t)\tau_p^i(t)}\cdot\right.\\
&\left.\gamma_q(t)\cdot c_{\text{b}}^i\left(t-\tau_q^i(t)\right)\cdot\text{e}^{\text{j}2\pi f_{\text{r},q}^i(t)t}\cdot\text{e}^{-\text{j}2\pi f_{\text{r},q}^i(t)\tau_q^i(t)}\right]\\
=\;&\int_T^{T+T_{\text{obs}}}\underbrace{\gamma_p^*(t)\cdot\gamma_q(t)}_{\substack{\Gamma_{p,q}(t)\\ \text{combined}\\ \text{hardware}\\ \text{influences}}}\cdot\underbrace{\left(c_{\text{b}}^i\left(t-\tau_p^i(t)\right)\right)^*\cdot c_{\text{b}}^i\left(t-\tau_q^i(t)\right)}_{\substack{C_{p,q}(t)\\ \text{decorrelation}\\ \text{through}\\ \text{delay}}}\cdot\\
&\underbrace{\text{e}^{-\text{j}2\pi\left(f_{\text{d},p}^i(t)-f_{\text{d},q}^i(t)\right)t}}_{\substack{D_{p,q}(t)\\ \text{differential Doppler}}}\cdot\underbrace{\text{e}^{\text{j}2\pi\left(f_{\text{r},p}^i(t)\tau_p^i(t)-f_{\text{r},q}^i(t)\tau_q^i(t)\right)}}_{\substack{A_{p,q}(t)\\ \text{Steering Vector}}}\text{d}t,
\end{aligned} \quad (41)$$

it can be seen that the correlation between the antenna signals can be separated into four terms, which are either dependent on the instantaneous delay or the change in delay during the observation interval, and are defined after Equations (6) and (7), respectively. As the antenna elements are fixed in a certain arrangement and cannot move independently, one can assess the decorrelation through delay by denoting the absolute value of the delay between two antenna elements as

$$\begin{aligned}
\left|\tau_{p,q}^i(t)\right| &= \left|\tau_p^i(t)-\tau_q^i(t)\right|\\
&= \left|\frac{\left(\boldsymbol{e}_{\boldsymbol{k}}^i\right)^{\text{T}}}{c_0}\left(\boldsymbol{r}_p(t)-\boldsymbol{r}_q(t)\right)\right| \le \frac{1}{c_0}\delta_{\text{ant,max}}.
\end{aligned} \quad (42)$$

It is obvious that the instantaneous delay is bounded corresponding to the largest distance $\delta_{\text{ant,max}}$ between two antenna elements, which can be assessed by the platform dimensions, ie, length and width of the car. Considering an example where the relative movement between the incident signal and the antenna elements p and q is constant, it holds that $f_{\text{d},p}^i(t) = f_{\text{d},q}^i(t) = f_{\text{d,c}}^i$. Thus, Equation (41) reduces using Equation (42) to

$$\begin{aligned}
&\text{E}\left[\left(c_p^i(t)\right)^*\cdot c_q^i(t)\right]\\
&= \gamma_p^*\cdot\gamma_q\cdot\text{e}^{\text{j}2\pi f_{\text{r}}^i\left(\tau_p^i-\tau_q^i\right)}\cdot\text{E}\left[\left(c_{\text{b}}^i(t)\right)^* c_{\text{b}}^i\left(t-\left(\tau_q^i-\tau_p^i\right)\right)\right]\\
&\le \gamma_p^*\cdot\gamma_q\cdot\text{e}^{\text{j}2\pi f_{\text{r}}^i\left(\tau_p^i-\tau_q^i\right)}\cdot\text{sinc}\left(f_{\text{b}}\cdot\frac{\delta_{\text{ant,max}}}{c_0}\right)
\end{aligned} \quad (43)$$

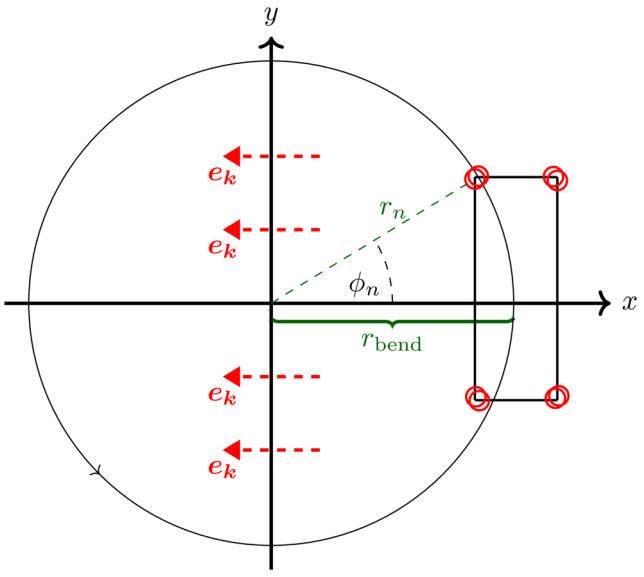

FIGURE 11 Position of the car, of the antennas (circles) and ϕ_n for $n = 1$ at $t = 0$ and the constant direction of the incident wave $\boldsymbol{e}_{\boldsymbol{k}}$ [Color figure can be viewed at wileyonlinelibrary.com and www.ion.org]

where f_b is the bandwidth of the complex baseband signal to be processed. As Equation (43) could be used to formulate an upper boundary for the signal bandwidth depending on the array dimensions for a stationary example, the motion-dependent parameters of Equation (41) raise further requirements on the observation interval T_{obs}. One can intuitively see that the Doppler dependent term $D_{p,q}(t)$ increases with increasing differential velocity between two antenna elements. Thus, one can assess the maximum decorrelation through movement by a pass through a curve, which delivers the aforementioned differential velocity of two antenna elements. The velocity of a car is thereby described by Feynman et al[15] as

$$v_{car} = \sqrt{a_{car} \cdot r_{bend}}, \tag{44}$$

where r_{bend} and a_{car} denote radius of the curve and the lateral acceleration, respectively.

The angular frequency of the car on the circular path can be expressed as

$$\omega_{car} = \sqrt{\frac{a_{car}}{r_{bend}}}, \tag{45}$$

which increases for a fixed a_{car} and decreasing radius. One can express the time-dependent position of antenna element n mounted onto the car with position $\boldsymbol{r}_{car} = [r_{bend}, 0, 0]^T$ at $t = 0$ using the estimated position from Equations (39) and (3) as

$$\boldsymbol{r}_n(t) = r_n \cdot \begin{pmatrix} \cos(\omega_{car} t + \phi_n) \\ \sin(\omega_{car} t + \phi_n) \\ 0 \end{pmatrix}, \tag{46}$$

where $r_n = ||\hat{\boldsymbol{r}}_n + \boldsymbol{r}_{car}||_2$ and $\phi_n = \text{asin}\left(\frac{\hat{r}_{n,y}}{r_n}\right)$ using the y-component of $\hat{\boldsymbol{r}}_n$. The resulting positions and the locus of the car are shown in Figure 11. The Doppler for source i is hence given with Equation (7) as

$$\begin{aligned} f^i_{d,n}(t) &= -f_t \cdot \frac{\dot{\boldsymbol{r}}^T_n(t) \cdot \boldsymbol{e}^i_{\boldsymbol{k}}}{c_0} \\ &= -\frac{\omega_{car} \cdot r_n \cdot f_t}{c_0} \cdot \begin{pmatrix} -\sin(\omega_{car} t + \phi_n) \\ \cos(\omega_{car} t + \phi_n) \\ 0 \end{pmatrix} \cdot \boldsymbol{e}^i_{\boldsymbol{k}}, \end{aligned} \tag{47}$$

whereas the delay is denoted by Equation (6). a_{car} can be expressed using the static stability factor[16] η as $a_{car} = \eta \cdot g$, where g is the acceleration through gravity, which is bounded for passenger cars and can be chosen to $\eta = 1$. To assess an upper limit on the observation time, we further choose a reasonable small value for the radius of the curve $r_{bend} = 13$m, resulting in $v_{car} = 40.63$ km/h. Finally, the vector of propagation of the incident wave $\boldsymbol{e}_{\boldsymbol{k}}$ is selected for $\phi^i = 0°$ and $\theta^i = 10°$ as a worst-case assumption, where the extents of the array relative to the direc-

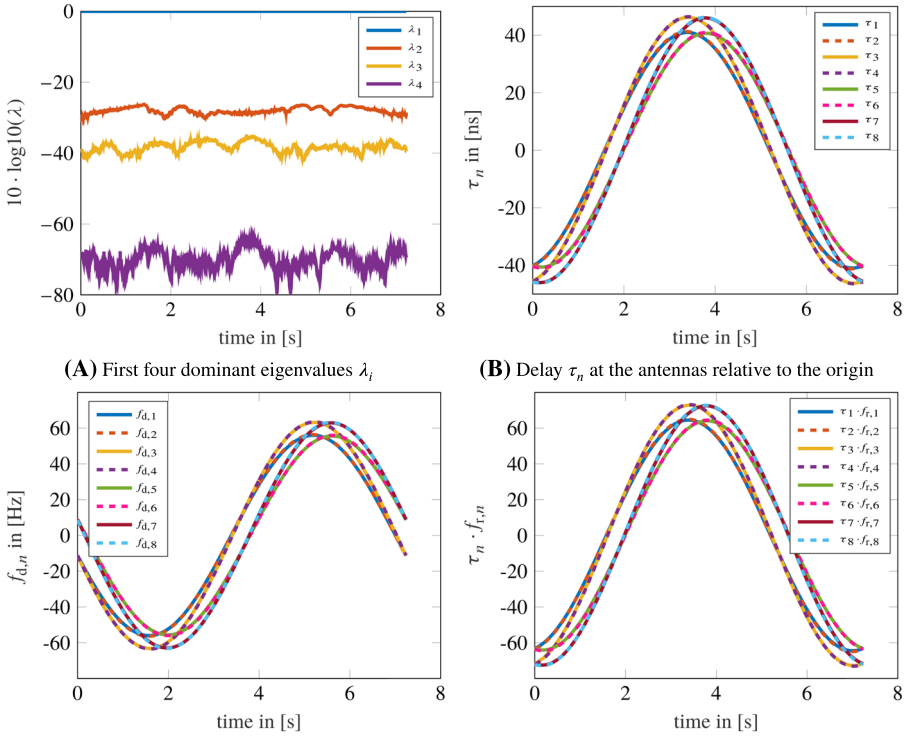

(A) First four dominant eigenvalues λ_i **(B)** Delay τ_n at the antennas relative to the origin

(C) Doppler $f_{d,n}$ at the antennas relative to the origin **(D)** Product of delay τ_n and received frequency $f_{r,n}$ relative to the origin

FIGURE 12 Illustration of the eigenvalues and the time-dependent parameters of Equation (41) over one rotation for $T_{obs} = 1$ ms and $f_b = 4$ MHz [Color figure can be viewed at wileyonlinelibrary.com and www.ion.org]

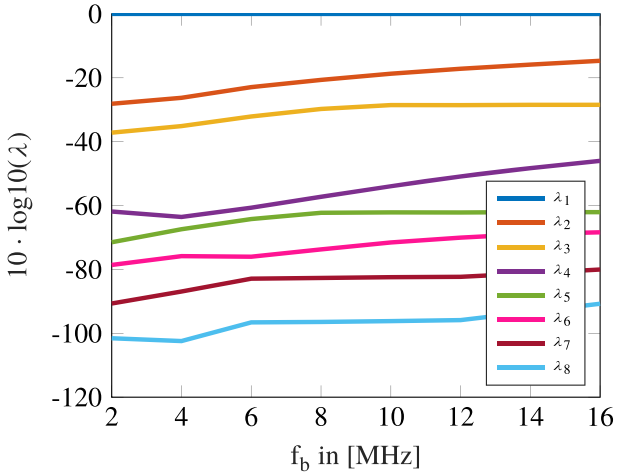

(A) Eigenvalues λ of the covariance matrix dependent on f_b for $T_\mathrm{obs} = 1$ ms

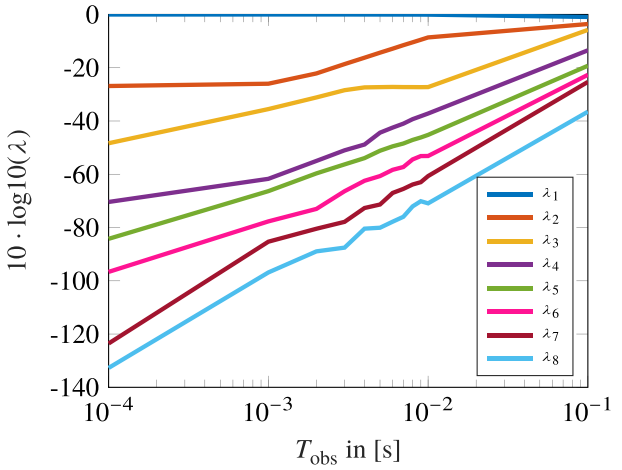

(B) Eigenvalues λ of the covariance matrix dependent on T_obs for $f_\mathrm{b} = 4$ MHz

FIGURE 13 Eigenvalues λ of the covariance matrix over f_b and T_obs [Color figure can be viewed at wileyonlinelibrary.com and www.ion.org]

(A) Array concept consisting of two sub-arrays (red circles) as proposed in Section 2 on the front bumper of a car (from left to right: antennas 4,3,2,1).

(B) Reference antenna (red circle) on top of the roof of the car

FIGURE 14 Antenna setup for the PVT measurement [Color figure can be viewed at wileyonlinelibrary.com and www.ion.org]

tion of the incident signal are largest, thus maximizing Equation (45), the difference in Doppler and the variation of $\hat{\boldsymbol{\gamma}}$ over T_obs.

The four dominant logarithmic eigenvalues of the covariance matrix as well as the delay τ_n, Doppler $f_{\mathrm{d},n}$, and the product of Doppler and received frequency $\tau_n \cdot f_{\mathrm{r},n}$ at the antenna signals as stated in Equation (41) are plotted for one rotation and the example of $T_\mathrm{obs} = 1$ ms and f_b in Figure 12. It shows that the movement of the car during the observation interval raises the second eigenvalue of the covariance matrix to about -30 dB. Depending on the interference to noise ratio, this leads to a further consumption of degrees of freedom in the interference mitigation stage and might be a problem for multiple incident jammers or in multipath scenarios.

Figure 13A,B shows the behavior of the eigenvalues in dependence of f_b for $T_\mathrm{obs} = 1$ ms and T_obs for $f_\mathrm{b} = 4$ MHz, respectively. In case of high bandwidths, the observation time needs to be significantly reduced to avoid a consumption of degrees of freedom, which in turn raises demands on the sampling rate f_s such that the block length to estimate the covariance matrix from Equation (21) is large enough to model the noise term $\boldsymbol{n}[k]$ as wide-sense stationary. Another conceivable countermeasure can be a reduction of velocity. As the scope of application is automated driving and the fact that a_car was chosen as a quite tough scenario, the illustrated effects are expected to be less severe most of the time.

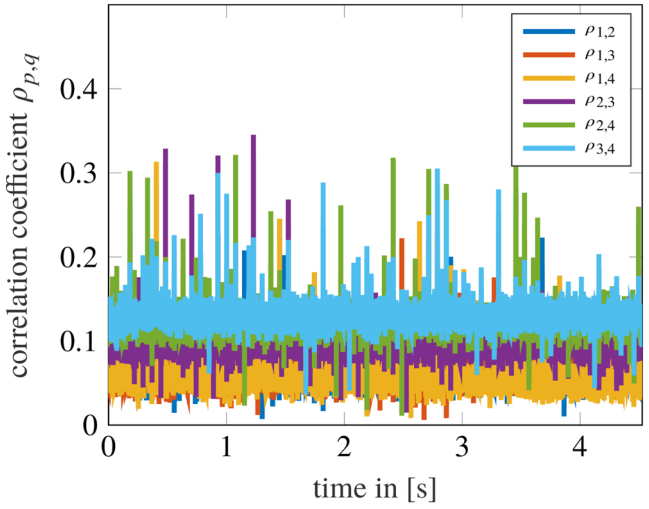

FIGURE 15 Correlation between the raw antenna signals from Equation (12) [Color figure can be viewed at wileyonlinelibrary.com and www.ion.org]

6 | EXPERIMENTAL VALIDATION OF POSITIONING ACCURACY

To verify the facilitation of the beamforming algorithms presented in Section 2 and demonstrate the benefit concerning the positioning solution using the proposed array design with distributed subarrays from Section 3, satellite signals were captured with an array consisting of four antenna elements in total as shown in Figure 14A, which was mounted onto the front bumper of a car. A fifth antenna is mounted on top of the roof of the car as shown in Figure 14B, whose signal is processed individually, and acts thus as a reference antenna in the following.

Note that the car from Section 4 is only used for the purpose of indoor antenna measurements; therefore, it lacks an engine and is inappropriate for the aspired measurement. Thus, to capture the data used for this section, it had to be replaced. Signals were captured at the L1 center frequency of $f_\mathrm{t} = 1.57542$ GHz with a bandwidth of $f_\mathrm{b} = 2$ MHz using an Ettus X300 Software Defined Radio (SDR) Platform with two TwinRX daughterboards and four commercially available NAVILOCK NL-202AA antennas. The signal from the reference antenna was captured with an Ettus B200mini SDR platform. Time and place of measurement was 7 October 2019 around 11 AM at a parking lot of the RWTH Aachen University at latitude 50.788152° and longitude 6.046864°. To assess the correlation of the raw antenna signals and to proof the assumption of uncorrelated spatial white noise from Equation (21), the cross-correlation coefficients between the raw antenna signals in $\boldsymbol{X}[\kappa]$ from Equation (15), which are block-wise evaluated, ie, the absolute values of the correlation coefficients

$$\rho_{p,q} = \left| \frac{1}{K-1} \sum_{k=\kappa}^{\kappa+K-1} \left(\frac{x_p[k] - \mu_p}{\sigma_p} \right)^* \cdot \frac{x_q[k] - \mu_q}{\sigma_q} \right|, \quad (48)$$

where μ_p and μ_q and σ_p and σ_q denote the mean values and standard deviations of $x_p[\kappa]$ and $x_q[\kappa]$, respectively, are shown in Figure 15. Despite outliers, the absolute values of $\rho_{p,q}$ do not exceed 0.2. Taking into account, that the raw antenna signals also include several weak, but correlated satellite signals, such that the correlation between the thermal noise signals is overestimated, the obtained results validate the assumption.

Figure 16 shows the position results using the arrangements from Figure 14 for two different trajectories, where the red color/dashed line indicates the results obtained from the reference antenna and the blue color/solid line shows the results derived from the array. For the results shown in Figure 16A, the car was moved on a straight path. Therefore, the received delays and phase differences between the individual antenna signals as stated in Equation (8) can be assumed to be approximately constant or at least slowly changing over the observation interval. Figure 16C,E compares the derived position results in latitude and longitude, respectively. It is remarkable that both estimations show comparable performance, whereas the latitude results of the reference antenna appear to have a slightly increased variance compared to the results derived from the array. Note that the peak in the latitude estimation around 11:25:30 MESZ appears for both outputs, but slightly later in the output of the reference antenna. This time instance belongs to the passage of the two trees in the middle of the trajectory as shown in Figure 16A, where the signals of satellites incident from a low elevation angle are distorted. The additional delay of this peak for the reference antenna can be explained from the orientation of the car and the arrangement of the array compared to the reference antenna as shown in Figure 14. The car moves from east to west, ie, from point 1 to point 2 in Figure 16A, such that the reference antenna passes the aforementioned point slightly later than the array.

However, the combination of signals from antenna elements at different positions seems to add no significant error to the positioning result in this example. Instead, it seems that the achieved gain in signal quality through the beamformer even improves the positioning result.

To test the array and the performance of the beamformers against platform rotations as explained in Section 5, a second trajectory as shown in Figure 16B is evaluated, where the car was moved on an "8"-shaped path.

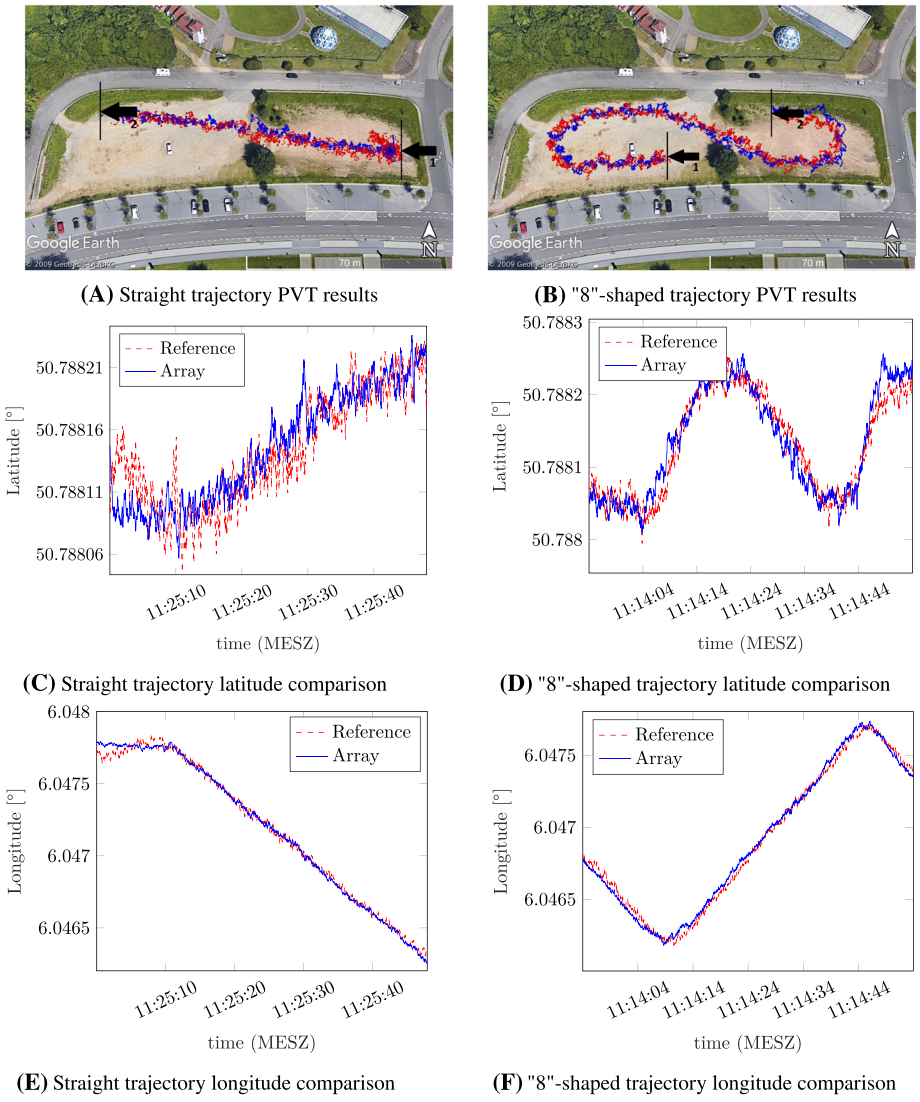

(A) Straight trajectory PVT results

(B) "8"-shaped trajectory PVT results

(C) Straight trajectory latitude comparison

(D) "8"-shaped trajectory latitude comparison

(E) Straight trajectory longitude comparison

(F) "8"-shaped trajectory longitude comparison

FIGURE 16 Comparison between the derived position estimates from the reference antenna element on top of the roof (red/dashed line) and the array (blue/solid line). Point 1 and point 2 denote the start and the end of the trajectory, respectively [Color figure can be viewed at wileyonlinelibrary.com and www.ion.org]

Thereby, the array is rotated over 360° on the complete interval. With this measurement, the effects described in Section 5, are tested for the eigenbeamformer, which is updated with a rate of $T_{\text{obs}} = 20$ ms. Figure 16D,F compares the estimations of latitude and longitude for this trajectory. Again, both outputs show comparable performance.

The results shown in Figure 16 demonstrate that the accuracy of obtained position results using the proposed array for the GPS L1 C/A system is comparable to those derived from a single antenna. The actual benefit of the approach lies in the opportunity to facilitate beamforming algorithms to suppress interferences and hence to navigate even in heavily degraded environments. However, at the time of writing, our chair waits on the permission to emit interference signals in the GNSS frequency bands. Thus, an experiment including an emitted interference signal is not possible at this point. Therefore, a white Gaussian noise sequence $\boldsymbol{z}^1(t)$ with bandwidth $f_{\text{b}} = 2$ MHz is added as an artificial interference signal to the raw antenna signals $\boldsymbol{x}(t)$ after Equation (12). The differential delays and phases between the individual antenna signals for $\boldsymbol{z}^1(t)$ as stated in Equation (9) are derived from the observation of a single satellite averaged over 1 second from the recorded antenna signals to preserve realistic signal characteristics for the generation of the artificial interference signals. Thereby, the parameters of the added signal at the individual antenna elements, ie, baseband delay τ_n and carrier phase offset for antenna n as explained in Equation (8), are derived to be as close to reality as possible with the intention to represent a realistic interference scenario. This has the big advantage that the effect of the interferer is based on measured signal characteristics instead of a model assumption, thus the mismatch between actually received and artificially generated signals is kept as small as possible.

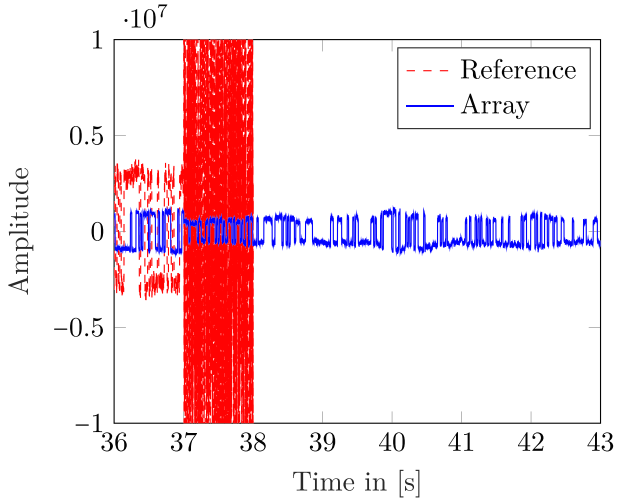

(A) Correlator output for the reference antenna and beamformed correlator output of the array for the satellite with PRN 32

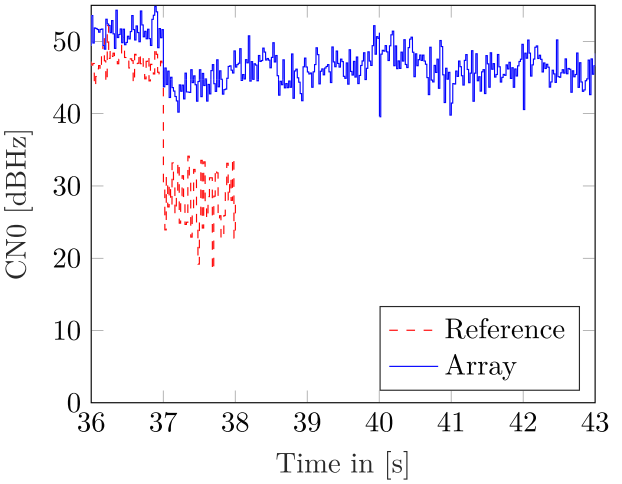

(B) Estimated carrier-to-noise-density ratio (CN0) from the correlator outputs of the satellite with PRN 32 as shown in Figure 17a

FIGURE 17 Comparison of the quality of the correlator output of the reference antenna and the beamformed correlator output of the array for the satellite with PRN 32 [Color figure can be viewed at wileyonlinelibrary.com and www.ion.org]

The amplitude $|z_n^1(t)|$ for antenna channel n is derived as

$$|z_n^1(t)| = \sqrt{10^{\mathrm{INR}/10} \cdot \overline{|x_n(t)|}^2} \tag{49}$$

where $\overline{(\cdot)}$ denotes the mean value. The interference to noise ratio is set to INR = 30 dB as used in Section 3. Using these parameters, a strong interference scenario with an assumed static interference source is generated.

The start of the interference signal is set to be 37 seconds after the start of the corresponding measurement. Figure 17A compares an example of the beamformed correlator output of the array $\tilde{d}_{\mathrm{bf}}(t)$ as stated in Equation (24) with the correlator output for the single antenna $\tilde{d}(t)$ for the "8"-shaped trajectory. One can see that immediately after the start of the interference, the correlator output of the single antenna consists only of noise. Therefore, the signal is lost after 38 seconds and cannot be re-acquired in the following, even though a reacquisition is performed every 2 seconds. This statement holds for all available satellite signals in the single antenna receiver. The consequences are on the one hand that the satellite ephemeris can no longer be decoded from the navigation message, and hence, the satellite positions cannot be determined. Even if those are available from another source, such as, for example, the internet, a pseudorange estimation is no longer possible.

The output of the array, however, shows only a drop in amplitude as the interference signal is mitigated through the prewhitening filter. The ephemeris data is correctly received until the end of measurement. The corresponding estimated carrier-to-noise-density ratios[17] (CN0) for that satellite are shown in Figure 17B. As the signal in the array only experiences a drop of about 5 dB, the CN0 drops from 45 dBHz to 30 dBHz, which corresponds to a signal loss.

Figure 18 shows the obtained position results for both aforementioned trajectories under the influence of the interference. The results are of course identical to those shown in Figure 16 until the interference source starts. One can see that the single antenna cannot tolerate the additional distortion from the interference source as the reception of all satellite signals is blocked as shown in Figure 17. Thus, it only delivers position estimates until 11:25:23 MESZ. The array however is able to mitigate the interference signal using the prewhitening filter as explained in Equation (22), which is updated with an interval of $T_{\mathrm{obs}} = 1$ ms. The position results of the array in latitude and longitude show for both trajectories a higher variance compared to the interference-free case after the start of interference. This demonstrates, that by accepting a slight increase in the variance of the estimated position, the navigation of an automatically driving car remains possible even under the influence of an interference, whereas a car with a single antenna would have no other possibility than to stop in that case.

7 | CONCLUSION

This paper demonstrated a new array design consisting of a minimum of two distributed linear subarrays. The influence of the distance and the orientation of the subarray combination on the ambiguity of the manifold of the

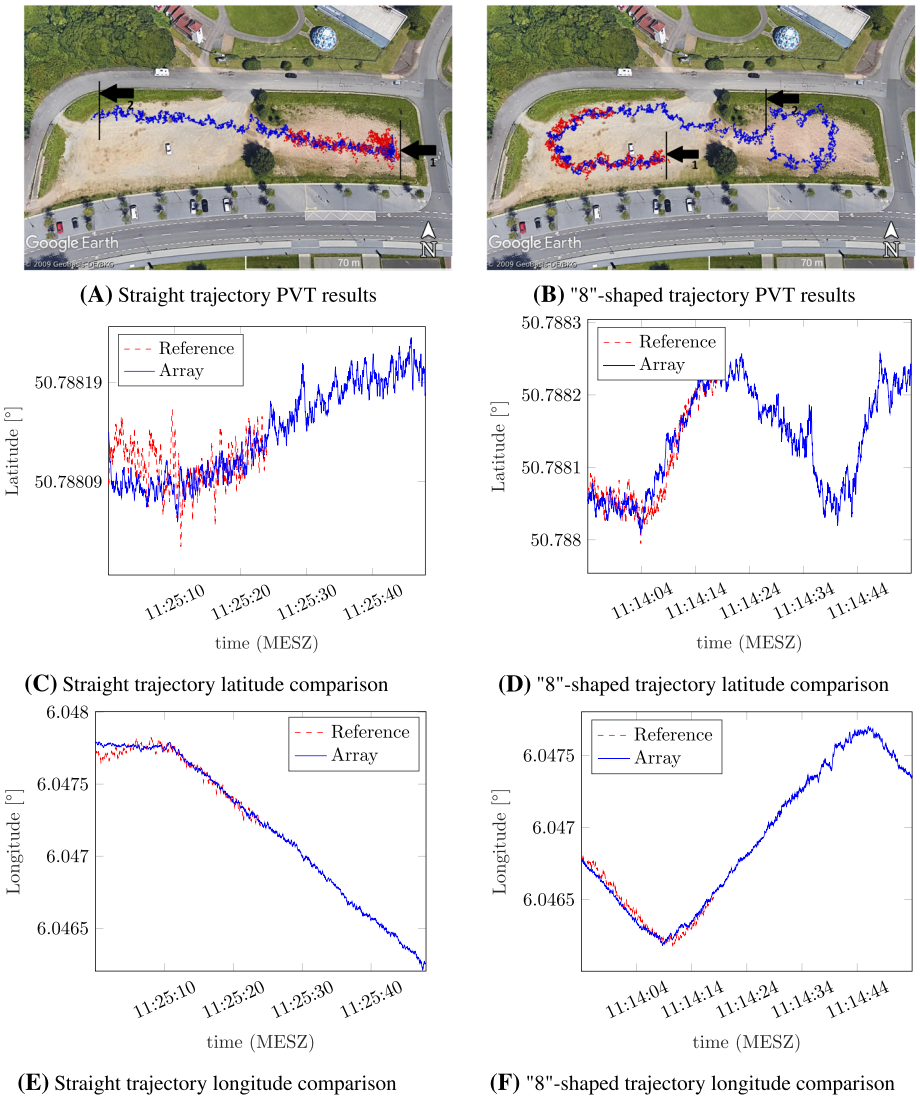

(A) Straight trajectory PVT results

(B) "8"-shaped trajectory PVT results

(C) Straight trajectory latitude comparison

(D) "8"-shaped trajectory latitude comparison

(E) Straight trajectory longitude comparison

(F) "8"-shaped trajectory longitude comparison

FIGURE 18 Comparison between the derived position estimates from the reference antenna element on top of the roof (red/dashed line) and the array (blue/blue solid line) for the case, where an interference source is switched on during the measurement. Point 1 and point 2 denote the start and the end of the trajectory respectively [Color figure can be viewed at wileyonlinelibrary.com and www.ion.org]

overall array has been analyzed, and constraints on both were derived. Through their reduced size, the combination seems appropriate for a hidden installation in the front and/or rear bumper of automobiles, which is an indispensable requirement by the industry. As the installation height is rather low, initial measurements of the attenuation through the metallic car body were presented for an exemplary array consisting of four distributed linear subarrays, each containing two antenna elements, which are mounted to the corners of a passenger car. It was shown that each subarray receives signals from three-fourths of the hemisphere, whereas signals incident from directions where the metallic car body obstructs the signal path are blocked at the corresponding subarray. Thus, every neighboring combination of two subarrays covers half of a hemisphere. The consequences of the obstruction by the metallic car body on amplitude and phase and the significantly higher array dimensions through signal delay and motion-dependent decorrelation on the interference mitigation stage were discussed, and increased demands on the integration time and the bandwidth of the incident signal for covariance matrix estimation were derived. To evaluate the influence of those effects on the quality of the positioning solution, signals from an array using the proposed design, which was mounted to the front bumper of a passenger car, were captured and processed through the proposed two-stage beamforming receiver. It was shown that code-based positioning results using only the GPS L1 C/A signal show comparable accuracy to a conventional single antenna receiver. However, the actual advantage of the proposed design lies in the aspect that a position determination is still possible under the influence of an interference source. As our chair currently awaits the permission to emit interference signals in the frequency bands of GNSS, an artificial interference signal was added to the measurement, which underlines the benefit of the array receiver: As the SINR of satellite signals in the single antenna receiver immediately drops, leading to a loss of all

satellite signals, the array receiver can tolerate the interference as it is capable of mitigating it spatially. The position results show a slightly increased variance compared to the interference-free case. However, using the proposed array, a global positioning solution can still be derived even in a heavily degraded environment, which is not possible for single antenna receivers. The proposed setup therefore solves two problems. First, allows for a concealed installation by maintaining the possibility to incorporate established methods for a spatial processing of incident signals to mitigate the impact of interferences, multipath, and/or spoofing signals. Second, even under adverse influences, the array allows for a code-based position determination using the L1 C/A code signal.

As high-accuracy solutions are desired especially in the field of automatic driving, the incorporation of further sensors by sensor fusion, such as, for example, inertial measurement units, will be tested at a later stage of development. Other sensors and techniques such as RADAR, LiDAR, and vision-based lane recognition algorithms can further improve the necessary accuracy for navigation. On the other hand, carrier-based positioning is aspired to be incorporated to obtain high-accuracy position results, which could, for example, be used in the interference-free case, and switching to array processing, if a jammer is detected. Research in this area is ongoing and will be assessed in a later publication.

ACKNOWLEDGEMENTS

Parts of the research leading to the results reported in this paper have been funded within the projects ROSANNA-Konzept and ROSANNA by the German Aerospace Center (DLR) on behalf of the German Federal Ministry for Economic Affairs and Energy under grant nos. 50 NA 1717, 50 NA 1718, 50 NA 1901, and 50 NA 1902. This support is greatly acknowledged.

ORCID

Marius Brachvogel https://orcid.org/0000-0003-1627-0278

REFERENCES

1. Pullen S, Gao G. GNSS Jamming in the name of privacy. *Inside GNSS*. 2012;2:34-43.
2. Cuntz M, Konovaltsev A, Sgammini M, Hattich C, Kappen G, Meurer M, et al. Field test: jamming the DLR adaptive antenna receiver. In: *Proceedings of the 24th International Technical Meeting of the Satellite Division of the Institute of Navigation (ION GNSS+ 2011)*. Portland, OR; September 2011:384-392.
3. Kurz L, Tasdemir E, Bornkessel D, Noll TG, Kappen G, et al. An architecture for an embedded antenna-array digital GNSS receiver using subspace-based methods for spatial filtering. In: *Proceedings of the 6th ESA Workshop Satellite Navigation Technologies (Navitec 2012) European Workshop GNSS Signals and Signal Processing*. 2012:1-8.
4. Tan KC, Goh SS, Tan EC. A study of the rank-ambiguity issues in direction-of-arrival estimation. *IEEE Trans Signal Process*. 1996;44:880-887.
5. Hein MA, Bornkessel C, Kotterman W, Schneider C, Sharma RK, et al. Emulation of virtual radio environments for realistic end-to-end testing for intelligent traffic systems. 2015:1-4.
6. Sleiman A, Manikas A. Antenna array manifold: a simplified representation. In: *Proceedings of the 2000 IEEE International Conference on Acoustics, Speech, and Signal Processing*. (Cat. No. 00CH37100), 2000;5:3164-3167.
7. Manikas A. *Array Ambiguities in Differential Geometry in Array Processing*. Imperial College Press; 2004. 113–156.
8. Zorn S, Niestroj M, Caizzone S, Brachvogel M, Meurer M. Self-contained antenna crosstalk and phase offset calibration by jointly solving the attitude estimation and calibration problem. In: *Proceedings of the 30th International Technical Meeting of the Satellite Division of the Institute of Navigation (ION GNSS+ 2017)*. Portland, OR; September 2017:3481-3493.
9. Zorn S, Saadi B, Niestroj M, Brachvogel M, Meurer M. Acurate position and attitude determination in a multipath environment using an uncalibrated multi-antenna-system. In: *Proceedings of the 31st International Technical Meeting of the Satellite Division of the Institute of Navigation (ION GNSS+2018)*. Miami, FL; September 2018:4027-4039.
10. Godara LC, Cantoni A. Uniqueness and linear independence of steering vectors in array space. *J Acoust Soc Am*. 1981;70:467-475.
11. Gialich M, Im A, Lee T, Aliyazicioglu Z, Hwang HK. DOA estimation using array antenna with large inter-element spacing. In: *2012 IEEE 11th International Conference on Signal Processing*, 2012;3:1701-1704.
12. Tan KC, Goh Z. A detailed derivation of arrays free of higher rank ambiguities. *IEEE Trans Signal Process*. 1996;44:351-359.
13. Tan KC, Goh Z. A construction of arrays free of rank ambiguities. In: *Proceedings of ICASSP '94. IEEE International Conference on Acoustics, Speech and Signal Processing*. 1994;4:545-548.
14. Hayward SD. Effects of motion on adaptive arrays. In: *IEE Proceedings - Radar, Sonar and Navigation*. 1997;144:15-20.
15. Feynman RP, Leighton RB, Sands M. Mechanik De Gruyter; 2015.
16. National Highway Traffic Safety Administration (NHTSA). Trends in the static stability factor of passenger cars, light trucks, and vans. *NHTSA Technical Report*; 2005.
17. Pini M, Falletti E, Fantino M. Performance evaluation of C/N0 estimators using a real time GNSS software receiver. *2008 IEEE 10th International Symposium on Spread Spectrum Techniques and Applications*. Bologna, Italy; 2008:32–36.

How to cite this article: Brachvogel M, Niestroj M, Zorn S, et al. A new array concept using spatially distributed subarrays for unambiguous GNSS interference mitigation in automotive applications. *NAVIGATION*. 2020;67:23–41. https://doi.org/10.1002/navi.353